Intradermal Needle-Free Powdered Drug Injection

by

John Liu

Submitted to the Department of Mechanical Engineering
in partial fulfillment of the requirements for the degree of

Master of Science in Mechanical Engineering

at the

MASSACHUSETTS INSTITUTE OF TECHNOLOGY

June 2012

Author .....
Department of Mechanical Engineering
May 21, 2012

Certified by .....
Ian W. Hunter
Hatsopoulos Professor of Mechanical Engineering
Thesis Supervisor

Accepted by .....
David E. Hardt
Chairman, Department Committee on Graduate Theses

Intradermal Needle-Free Powdered Drug Injection

by

John Liu

Submitted to the Department of Mechanical Engineering
on May 21, 2012, in partial fulfillment of the
requirements for the degree of
Master of Science in Mechanical Engineering

Abstract

This thesis presents a new method for needle-free powdered drug injection. The design, construction, and testing of a bench-top helium-powered device capable of delivering powder to controllable depths within the dermis is presented. This device uses a jet of gas undergoing choked flow to entrain powder and subsequently penetrates through the skin for delivery of the powder. Different nozzle designs and orifice geometries are also explored. *In vitro* injection of polymer beads (1–5 μm in diameter) into porcine tissue demonstrate the device's capability of drug delivery to depths of 260 to 5000 μm. The jet parameters of nozzle orifice diameter and applied pressure are shown to affect injection depth, shape, and success rate. The presented device has the potential to be implemented with stabilized formulations of vaccines to address the cold chain problem—the cost and risk of transporting temperature sensitive vaccines to developing countries.

Thesis Supervisor: Ian W. Hunter
Title: Hatsopoulos Professor of Mechanical Engineering

Acknowledgments

First, I would like to express my heartfelt gratitude towards my advisor Professor Ian Hunter for giving me the opportunity to research in his lab. The scientific development I have experienced in these past two years would not have been possible without the guidance and encouragement he has given me.

I would also like to thank Dr. Cathy Hogan for her dedication and support. Dr. Hogan spent countless hours guiding my next step in experimentation, providing advice on biology, and training me in the biological experiments necessary for my research. Thank you to Ms. Kate Melvin for helping me manage my lab materials so that my research could continue without unnecessary hitches.

I would like to thank Bryan Ruddy and Yi Chen for their invaluable advice, ideas, and optimism. When faced with an engineering problem, they had the uncanny ability to turn on just enough light for me to start moving again. I would also like to thank other colleagues in the Bioinstrumentation Lab: to Jean Chang for her commitment and care in editing this thesis, to Brian Hemond, Adam Wahab, and James White for insightful discussions, and to Ashley Brown, Alison Cloutier, Ashin Modak, and Adam Spanbaeur for all of the heartfelt laughter in lab. I would like to thank a UROP in the lab, Rachel Dias Carlson, for helping me with the tissue sectioning work.

This research was supported in part through the NSF Graduate Research Fellowship and Sanofi S.A.

Thank you to my friends in the Christian community at MIT and Park Street Church for displaying to me what love looks like. They have been to me a home away from home.

To Elizabeth and Esther, a cord of three strands is not easily broken. I thank God for blessing me with two of the loveliest sisters in this world.

To Dad and Mom, words simply cannot express my gratitude. It is hard to imagine a set of parents more loving, godly, and dedicated than you are.

And lastly to Jesus Christ, You are my soul's glory, joy, and crown.

Contents

List of Figures

List of Tables

Chapter 1

Introduction

1.1 Global Vaccination

Vaccine immunization saves more than three million lives worldwide each year [1] and is considered to be one of the most cost effective measures of addressing disease on a global scale. Over 100 million children below the age of one are immunized against measles, polio, and other diseases [2, 3]. There remain areas for great improvement, namely the cold chain—the temperature controlled supply system of vaccines stored at temperatures of 2–8 °C—which is one of the most vulnerable aspects of vaccine delivery for the developing world. Numerous studies across different countries [4] show frequent refrigeration malfunction that leads to drug waste, vaccinations administered with compromised vaccines, and an increased financial cost of 200–300 million dollars a year [5]. Furthermore, vaccination using a needle and syringe poses serious global health problems. When compared to health workers in the United States and Canada, the average number of sharps injury per worker per year is over 26 times higher (4.7 sharps injuries per healthcare worker per year compared to 0.18) in countries such as Egypt and Pakistan [5].

To alleviate the problems currently associated with the cold chain, different approaches have been investigated. Efforts such as the World Health Organization's vaccine vial monitor (VVM) and new refrigeration and temperature monitoring technologies have offered some improvement [6]. Lyophilization of vaccines is well doc-

umented and has improved the shelf life of many formulations but the lyophilized drug still needs to be refrigerated. Reformulating drugs to be thermostable between the temperatures of freezing and 45 °C by methods such as spray drying and spray freeze drying are currently being developed. In particular, a recent study showed that spray-dried formulations of the Hepatitis B vaccine were stable for at least 24 months at 37 °C [7]. The development of the delivery of thermostable powder vaccines leads to the potential of eradicating the need for cold chain supply and transportation.

1.2 Needle-Free Vaccine Delivery Systems

Needle-free vaccine delivery systems have garnered a heightened interest in the past few decades. The advantages of needle-free delivery are numerous. Elimination of the needle eliminates the risk of sharps injury and cross-contamination through re-use of the needle while removing the need for sharps disposal, solving the issue of needle phobia, and increasing patient compliance. Numerous methods of needle-free drug delivery have drawn the interest of research and commercial groups and can be grouped into two general types based on the location of delivery: mucosal and cutaneous administration.

Administration of drug to the mucous membranes covering the aerodigestive or urogenital tracts (e.g. to oral, nasal, pulmonary, vaginal, or rectal sites) intuitively is an effective method of vaccine delivery since pathogens of major diseases such as HIV or the influenza virus enter the body through mucosal tissue. The mucosal immune system contributes nearly 80% of a healthy adult's immunocytes and is therefore sensitive to antigens. Thus, many methods to target sites in the mucosal immune system are in development. However, delivery via each route currently has major constrictions that limit its usage. For example, while oral delivery of drugs has a high patient compliance rate, because of the poor stability of proteins in an acidic and enzyme-rich environment, non-living vaccines tend to break down in the gastrointestinal tract [8]. Similarly, aerosolized vaccines delivered to the nasal site are less likely to break down due to lower enzymatic activity, but there are still constraints on the size of the ac-

tuated droplet and medicinal agent for proper placement of the deposited drug and avoidance of inflammatory responses [9].

To offer an alternative to the needle and syringe, other methods of cutaneous delivery are being developed: topical application, microneedles, and needle-free injection. Topical delivery of vaccines (Figure 1-1c) is attractive because of the high density of antigen-presenting cells in the superficial layer of the skin, but permeating through the stratum corneum has traditionally been a challenge. To alleviate this problem, hydration, mechanical (e.g. abrasion to physically disrupt the stratum corneum), and chemical methods (adjuvants or permeabilizing agents) are used to increase the permeability of the stratum corneum to drug molecules. Each of these methods comes with its unique advantage and disadvantage [5, 8]. Microneedles (Figure 1-1h) (solid and hollow arrays of silicon projections 25 to 1000 μm long) are designed to specifically penetrate the stratum corneum into the epidermal and dermal layer, yet are designed to be short enough to avoid contacting nerves found in the fat layer. The joint usage of the microneedle and transdermal patch show promising results in recent clinical trials [10] but may still not be appropriate for mass immunizations due to their two-step application of microneedle and patch.

Finally, needle-free injection is a technology that propels the drug in a high-velocity stream of fluid to penetrate the tissue, effectively replacing the needle with the drug itself. In the 1950s to the 1980s, the United States military used multi-use-nozzle jet injectors (MUNJIs) to administer mass immunizations to its personnel [8]. However, injector tips were not changed upon each injection, leading to the exchange of bodily fluids from one recipient of the vaccine to another. This practice led to a widespread cross-contamination of Hepatitis B [8]. In the last two decades, independent health care groups, non-governmental organizations, and biotech companies have been independently developing a variety of different devices, such as the commercially available Biojector 2000 [11] and Injex [12] (Figure 1-2 a and b). However these devices offer low controllability of the depth of delivery due to their actuation mechanisms' (spring and gas, respectively) inabilities to shape their pressure profiles. A recent improvement of this technology took place in MIT's Bioinstrumentation

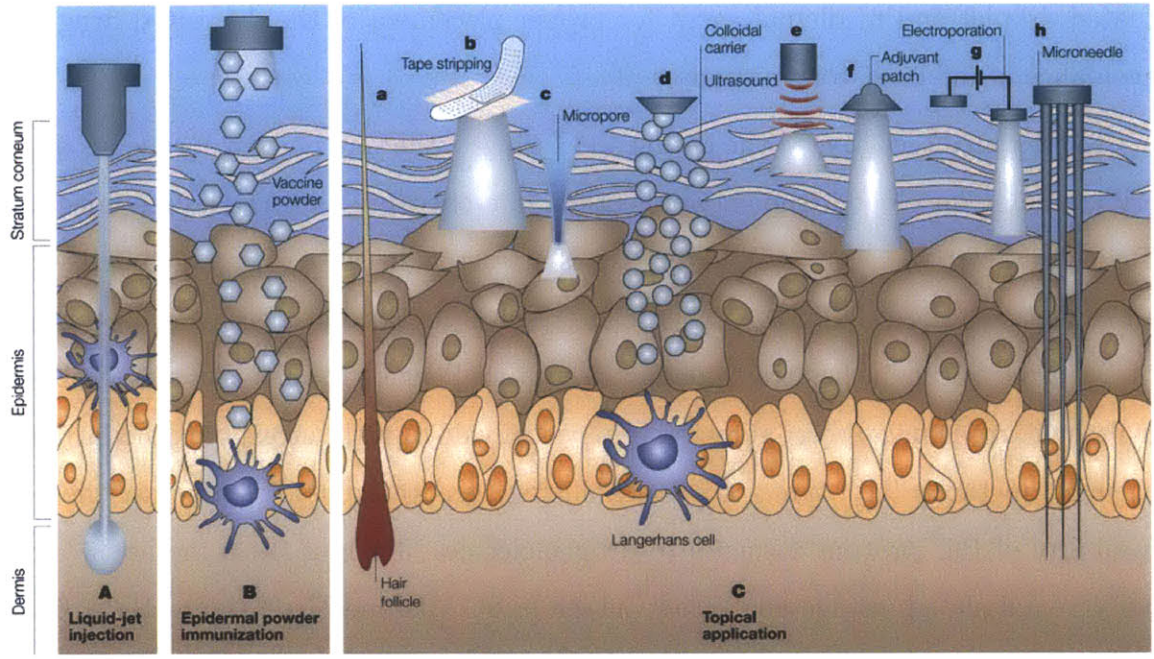

Figure 1-1: Various current methods of cutaneous immunization. Taken from Mitragotri, et al. [8].

Lab. A highly controllable Lorentz-force actuator called a "jet injector" (JI) (Figure 1-2c) was developed to use a two-phase pressure profile to repeatedly deliver a pre-determined volume of drug to controllable depths in the tissue [13].

Virtually all current needle-free injection systems use aqueous solutions, which require reconstitution of the powdered drug. Because a reconstituted drug is thermally unstable, unused reconstituted drugs must be disposed of after 24 hours, leading to drug wastage [14]. If powdered vaccines can be delivered directly, there will be no need for diluent and reconstitution, further cutting costs in storage, transportation, and human training and error.

To date, few powder injection systems have been developed. A helium-powered needle-free technology [15] is able to perform epidermal powder immunization (EPI) [16]. However, because particle penetration is governed by the ballistics of individual particles, constraints exist on the size and density of each particle for it to achieve momentum density sufficient for penetration. Because of these constraints, standard pharmaceutical formulation techniques may need to be modified [17] and this tech-

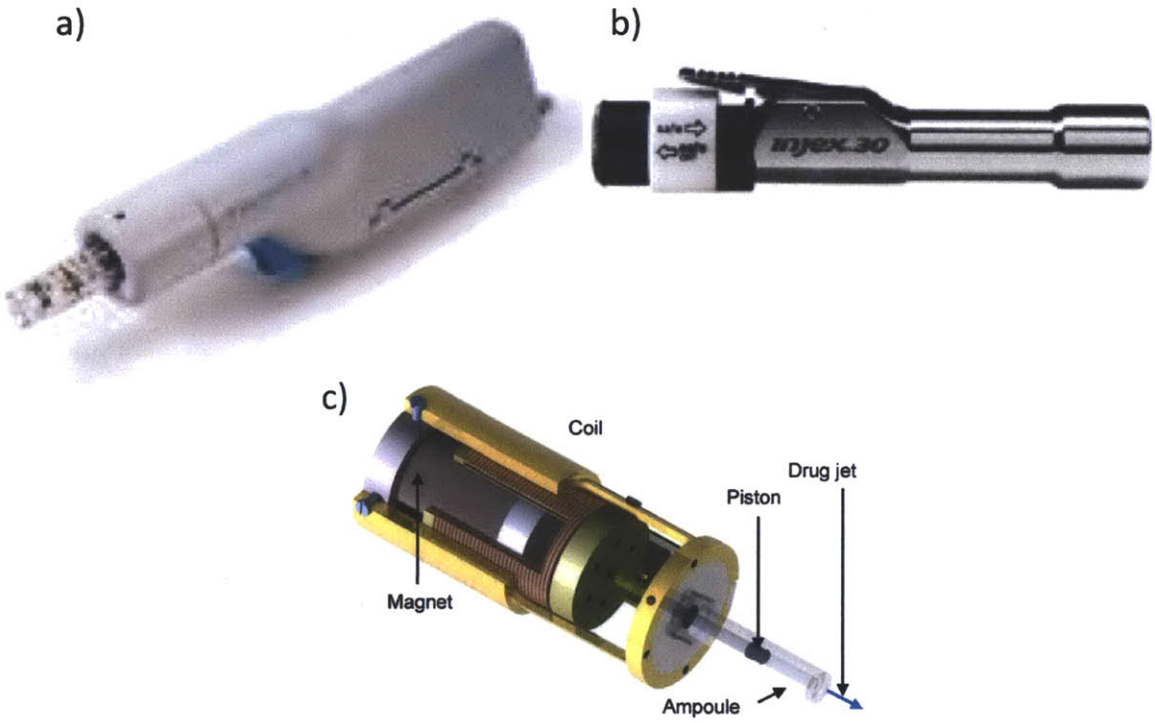

Figure 1-2: a) Picture of the Biojector 2000. Taken from the Bioject website [11]. b) Picture of the Injex. Taken from the Injex website [12]. Cutaway view of the linear Lorentze-force actuator of the MIT Bioinstrumentation JI. Taken from Taberner, et al. [13].

nology may not be ideal in situations where financial resources are limited.

This thesis describes the design, construction, and testing of a needle-free drug delivery device used to inject powder to controllable depths. The development of this new method of drug delivery could find its application in the developing world and help alleviate issues associated with the cold chain.

1.3 Description of Chapters

This thesis is organized as follows:

Chapter 2 lays a framework for understanding a jet composed of gas and powder by elucidating the jet mechanics and choked flow of compressible fluids. These calculations are also compared to previous work in powder delivery.

Chapter 3 describes the development of a helium-powered device to perform powder injection. Various nozzle designs are also developed.

Chapter 4 describes the characteristics of the helium-powered device.

Chapter 5 reports the results of powder injection *in vitro*. The device's ability to control injection depth, shape, and success rate are presented.

Chapter 6 presents a brief summary of the work presented in this thesis and future areas of work.

Chapter 2

Background

We hypothesize that if entraining powder into a gas jet is possible, the subsequent two-phase mixture could be delivered into the tissue. We would like to draw from both an understanding of aqueous drug delivery by a liquid jet and powder ballistic delivery by a carrier gas to motivate powder delivery by a gas jet.

2.1 Mechanics of Liquid Jet Delivery

Shergold, et al. [18] hypothesized two phases in liquid jet injection: the initial penetration of the skin by a jet at high velocity and subsequent delivery of the bulk of the liquid. They described skin penetration by liquid jet using the "sharp-tipped punch penetration model" [18]. This model describes that penetration of a soft solid by a sharp-tip solid object involves cracking the soft solid, and upon the removal of that object the tissue undergoes reversible deformation to close the crack. This model predicts that for liquid jets of diameters ranging from 100 to 500 μm, a peak pressure of 14 MPa is sufficient for skin penetration, though other literature has suggested that the critical yield stress for the stratum corneum has a larger range: 3.2–22.5 MPa [19].

Based on the observation that both exit velocity and nozzle diameter influenced the depth of drug delivery in jet injections, Schramm-Baxter, et al. [20] used the concept of "jet power" (P_0) to describe a jet of fluid. For a liquid jet accelerated

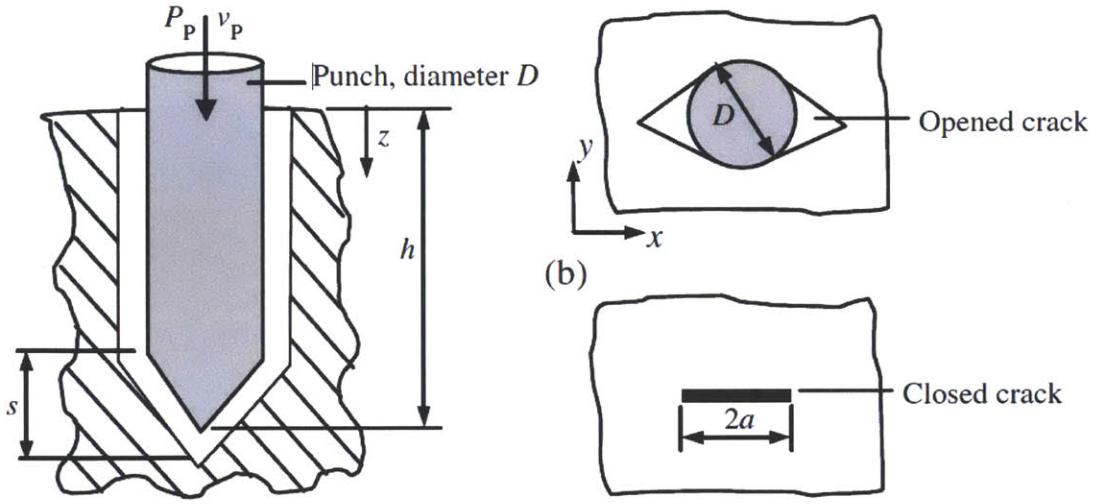

Figure 2-1: The sharp-tipped punch model. Figure taken from Shergold, et al. [18].

some distance away from the surface of the tissue, they found that increasing the jet power of a jet injection increases both the depth of the erosion hole created by the injection and depth of the fluid dispersion in the tissue (Figure 2-2).

Assuming a constant velocity profile across the orifice,

$$P_0 = \frac{1}{2}\dot{m}u_0^2, \tag{2.1}$$

where $\dot{m}$ is the mass flow rate, and u_0 is the exit jet velocity.

The mass flow rate is related to u_0 by

$$\dot{m} = \rho A_0 u_0, \tag{2.2}$$

where ρ is the fluid density and A_0 is the area of the nozzle orifice. Then

$$P_0 = \frac{1}{8}\pi\rho D_0^2 u_0^3, \tag{2.3}$$

where D_0 is the diameter of the jet [20].

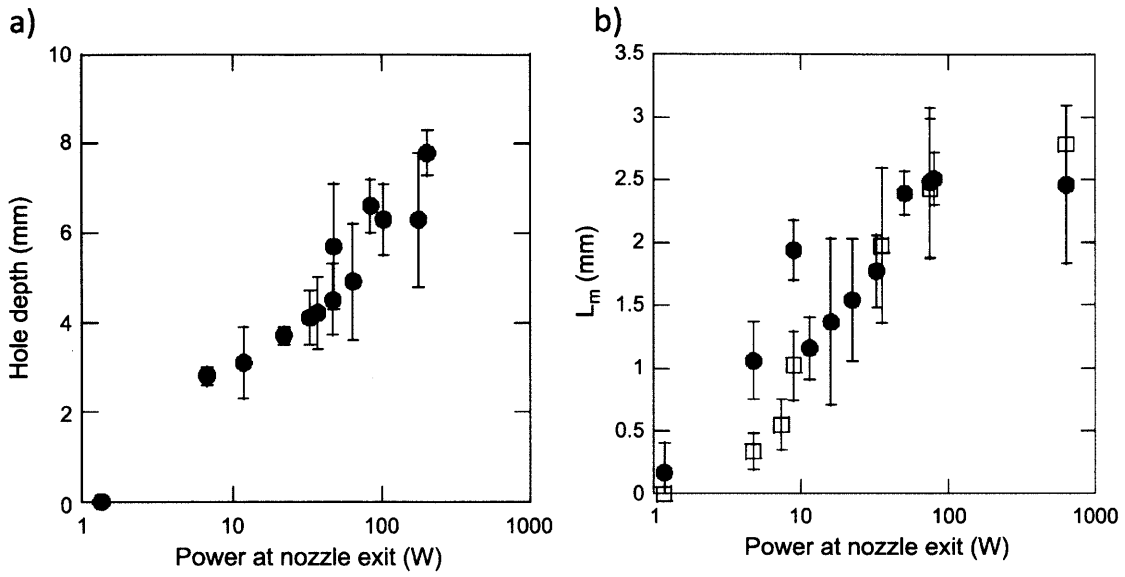

Figure 2-2: Jet power describes liquid jet injection behavior well: a) Dependence of the depth of the erosion hole that a liquid jet creates, on jet power. b) Dependence of L_m, the depth corresponding to the maximum width of dispersion in the tissue, on jet power. Figures taken from Schramm-Baxter, et al. [20].

2.2 A Prior Art: Powder Ballistic Delivery

In ballistic drug delivery as used in epidermal powder immunization (Figure 2-3), individual particles are accelerated by a carrier gas, which is typically helium. Upon skin impact, the gas is deflected, leaving the individual particles to penetrate the stratum corneum and deposit into the viable epidermis. The depth of an individual particle's successful penetration into the viable epidermis is dependent on the conversion of its kinetic energy into the kinetic energy of the tissue (the inertia of the particle transferring to the tissue as it bends) and the subsequent plastic deformation of penetration into the tissue [21].

Three parameters of the particle have been found to affect the penetration depth: the particle's density (ρ_p), diameter (r_p), and impact velocity (v_i). To combine the information of these three parameters, they are multiplied together ($\rho v_i r_p$) to form "momentum density," the impact momentum per cross-sectional area of the particle. In successful penetrations, typical momentum densities of particles are in the range

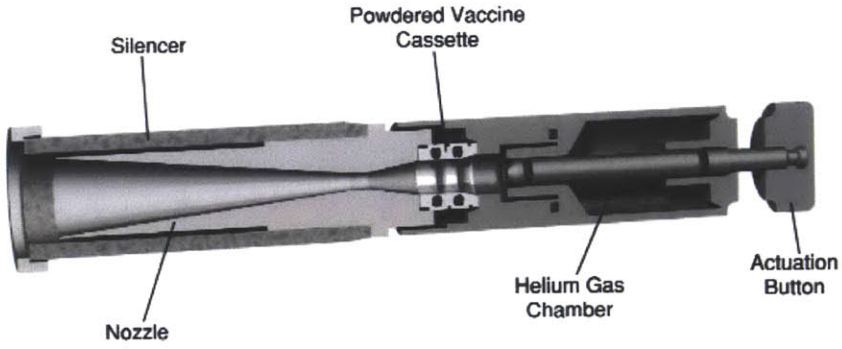

Figure 2-3: Picture of the Powderject device for epidermal powder immunization. Figures taken from Chen, et al. [16].

of 7 to 14 kg/m · s, below which particles do not penetrate the stratum corneum [21].

2.3 Calculations for a Jet Composed of Gas and Powder

We would like to answer two questions:

1. What parameters are needed for a jet composed of gas and powder to be "similar" to a jet composed of liquid?

2. If one can deliver powder via a jet of gas and powder, how does it compare to ballistic delivery?

2.3.1 Gas Flow Mechanics

To gain some intuition about how a jet composed of gas and powder might behave, we first analyze the mechanics of the gas, and perform an analysis of compressible fluid flow from a convergent nozzle (Figure 2-4) into atmospheric surroundings (no load is placed against the nozzle).

We start by assuming a peak pressure of 10 MPa, a pressure on the order of common peak pressures found in liquid injections. We note that the ratio of the back

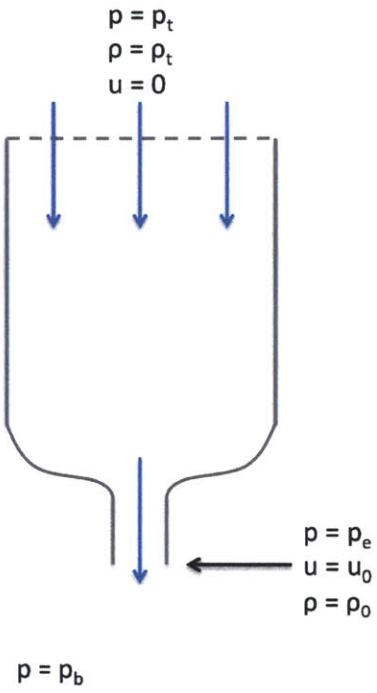

Figure 2-4: Diagram of the nozzle for compressible fluid flow.

pressure at atmospheric (p_b = 101,325 Pa) to total pressure at peak ($p_t = 10 \cdot 10^6$ Pa), p_b/p_t, is less than the ratio of the critical pressure to total pressure at peak, p_*/p_t [22]. That is,

$$0.010133 = \frac{101325}{10 \cdot 10^6} = \frac{p_b}{p_t} < \frac{p_*}{p_t} = (\frac{2}{\gamma + 1})^{\gamma/(\gamma-1)} = 0.488, \tag{2.4}$$

where γ is the adiabatic constant (5/3 for helium). Equation 2.4 is the criteria for choked flow ($p_b/p_t < p_*/p_t$) and because it is met we know that the velocity of the gas jet at the nozzle orifice is "choked" at the speed of sound ($u_0 = v_{sound}$). In fact, for an ejection of gas into the surroundings held at atmospheric pressure, any increase of applied pressure beyond p_* = 101,325/0.488 = 207,633 Pa, will not increase the velocity of the gas.

The speed of sound is described by,

$$v_{sound} = \sqrt{\frac{\gamma RT}{M}}, \tag{2.5}$$

where R is the gas constant (R = 8.314 J/mol $\cdot$ K) and M is the molecular mass ($4.04 \cdot 10^{-3}$ kg/mol for helium). Then at T = 293 K the speed of sound for helium (v_{sound}) is:

$$v_{sound} = \sqrt{\frac{1.66 \cdot 8.314 \cdot 293}{M}} = 1007 \text{ m/s}. \tag{2.6}$$

When the gas velocity is choked, the equation for the mass flow rate ($\dot{m}$) [23] is:

$$\dot{m} = CA\sqrt{\gamma \rho_t p_t (\frac{2}{\gamma+1})^{(\gamma+1)/(\gamma-1)}}, \tag{2.7}$$

where ρ_t is the gas density at the source. Because of compressible flow, we must make a distinction between the gas density at the source ρ_t and gas density at the orifice exit ρ_0. To find ρ_t, we apply the ideal gas law:

$$\rho_t = \frac{p_t M}{RT} \tag{2.8}$$

$$= \frac{10 \cdot 10^6 \cdot 0.0040026}{8.314 \cdot 293} = 16.43 \text{ kg/m}^3. \tag{2.9}$$

To find ρ_0, we combine Equations 2.2 and 2.7:

$$\rho_0 = \frac{C}{v_{speed}}\sqrt{\gamma \rho_t p_t (\frac{2}{\gamma+1})^{(\gamma+1)/(\gamma-1)}}, \tag{2.10}$$

where C is the coefficient of discharge (0.60 for a sharp edge orifice) and keeping in mind that $u_0 = v_{speed}$ for choked flows.

Then combining the expression for exit density (ρ_0) from Equation 2.10 and jet power (P_0) from Equation 2.3, we obtain an expression for the jet power of a compressible fluid jet experiencing choked flow:

$$P_0 = \frac{\pi}{8} D_0^2 v_{sound}^2 C\sqrt{\gamma \rho_t p_t (\frac{2}{\gamma+1})^{(\gamma+1)/(\gamma-1)}}, \tag{2.11}$$

or substituting the expression for ρ_t from the ideal gas law (Equation 2.9):

$$P_0 = \frac{\pi}{8} D_0^2 v_{sound}^2 C p_t \sqrt{\frac{\gamma M}{RT}} (\frac{2}{\gamma+1})^{(\gamma+1)/(\gamma-1)}. \quad (2.12)$$

The rupture of skin by a macroscopic object is dependent on attaining critical yield stress [18] and thus the application of sufficiently high pressure and jet power using any medium would rupture the tissue. However, because of the dependence of delivery depth on the jet power of a liquid jet as elucidated in Section 2.1, we will use jet power as a metric for performing similar injections by a jet composed of gas and powder.

The jet parameters of a typical jet injection are: $\rho = 1000$ kg/m^3, $D_o = 200$ μm, and $u_0 = 200$ m/s. From Equation 2.3 this yields a jet power of:

$$P_0 = \frac{1}{8}\pi(1000)(200 \cdot 10^{-6})^2(200)^3 = 125.7 \text{ W}. \quad (2.13)$$

Then given Equation 2.11, we see that the jet power of a gas jet of the same diameter experiencing a peak pressure of 10 MPa is:

$$\begin{aligned} P_0 &= \frac{\pi}{8} \cdot (200 \cdot 10^{-6})^2 \cdot (1007)^3 \cdot (0.60) \cdot \\ &\quad \sqrt{(1.66)(16.43)(10 \cdot 10^6)(\frac{2}{1.66+1})^{(1.66+1)/(1.66-1)}} \quad (2.14) \\ &= 88.84 \text{ W}, \quad (2.15) \end{aligned}$$

which is similar to the jet power calculated for liquid injection (Equation 2.13).

2.3.2 Comparison of Ballistic Powder Delivery to Powder Delivery by a Gas Jet

If typical polystyrene beads (1–5 μm, 1500 kg/m^3) can be entrained in the gas jet described in Section 2.3.1 ($v = 1007$ m/s), this yields a range of momentum densities from 1.5 to 7.5 kg/m $\cdot$ s, in general lower than the range of momentum densities of ballistically delivered particles.

Since skin puncture would be solely dependent on the stress induced by the jet, if a device can entrain powder into the gas jet to form a jet composed of gas and powder, then delivery of solid particles of lower momentum density (and therefore less restrictions on the formulation of the drug) can be delivered.

Chapter 3

Device Development

3.1 Design Parameters

The main purpose of this research was to develop a new method of injecting powder into tissue to controllable depths. The device was developed according to the following guidelines:

1. The method would not use liquid in any phase of the injection.
2. Gas would be used to entrain the powder in its stream.
3. The powder would be accelerated to sub- or sonic speeds.

3.2 Bench-top Setup

To fulfill this purpose, a high-pressure pneumatic valve system was conceived and implemented in a bench top setup. The bench top setup (Figure 3-1) is composed of a high-pressure stainless steel solenoid valve (Parker model 71216) connected to a tank carrying industrial-grade helium (Airgas HE40) by a smooth-bore stainless steel gas hose (Unisource 4TSC-11-11-36.0) and outfitted pressure regulator (Airgas E13-N115H). A pressure sensor is attached between the pressure regulator (Omega model PX303-4KG5V) and hose to determine the applied pressure at the nozzle.

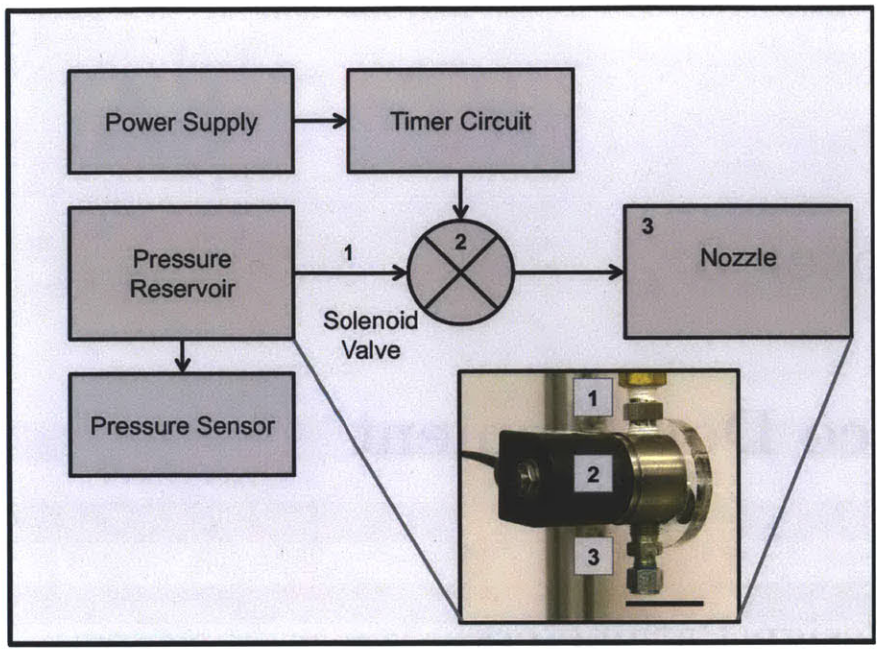

Figure 3-1: Block diagram of the bench-top powder injector and (inset) photograph of the device: gas flows from the gas tank through the hose (1) to the solenoid valve (2) and to the nozzle (3) (scale bar = 30 mm).

3.3 Carrier Gas

Helium was chosen as the carrier gas because of its comparatively high diffusivity in tissue and low solubility in blood [24]. We conjecture that injection of helium into the upper layers of tissue poses minimal risk of enducing embolism. This issue is addressed by qualitative observation in Section 5.3 though further quantitative studies are needed to verify such a hypothesis.

Because previous needle-free liquid injection experiments utilized peak pressures of 10–20 MPa to penetrate tissue, it was decided to use a standard helium tank, yielding maximum pressures of 14 MPa.

3.4 Electronics

A timer circuit (Figure 3-2) designed by Bryan Ruddy, a PhD candidate in the lab, was used to control the solenoid valve. In its deactivated state, the coil inputs (W3

and W4) are both kept at the constant voltage of 24 V. When the circuit to the power supply is connected via an external switch (W1 and W2) it introduces a voltage difference across the Precision Timer (SE555), which sends a timed pulse of control current to the MOSFET driver (TC4420). The MOSFET driver then sends a timed pulse of amplified current to the MOSFET (IRFB3077) which connects the negative terminal of the coil input (W4) to the ground rail for a pre-determined time. The solenoid valve is connected to the coil inputs and is thereby energized by a timed voltage pulse of 24 V from the power supply. A voltage pulse width of 15 ms was used as the duration of the voltage pulse to be analogous to the widths of the pressure peaks in typical liquid needle-free injections.

3.5 Powder

White glass beads (1000 kg/m^3, 2–10 μm) and colored fluorescent beads (1500 kg/m^3, 1–5 μm) were chosen to simulate drug delivery as they have similar densities and particle sizes to that of lyophilized drug [17, 25].

3.6 Nozzle

At the time of this research, no commercial nozzles were easily adaptable for powder injection; thus various attempts were made to custom-design and create nozzles for powder injection. The purpose was to machine nozzles that withstood high levels of pressure (up to 14 MPa) with orifice diameters ranging from 50–200 μm.

3.6.1 Stereolithography Produced Nozzle

A nozzle was fabricated by stereolithography (SLA) using the Viper Si2 [26] and is shown in Figure 3-3. During the fabrication process, the nozzle tip was found to be without orifice before curing. It is likely that the resin does not vent from the orifice because of its narrowness. In order to form the orifice, a 150 μm minuten pin (shown in Figure 3-3b) was manually inserted into the soft resin, cured, then removed post-

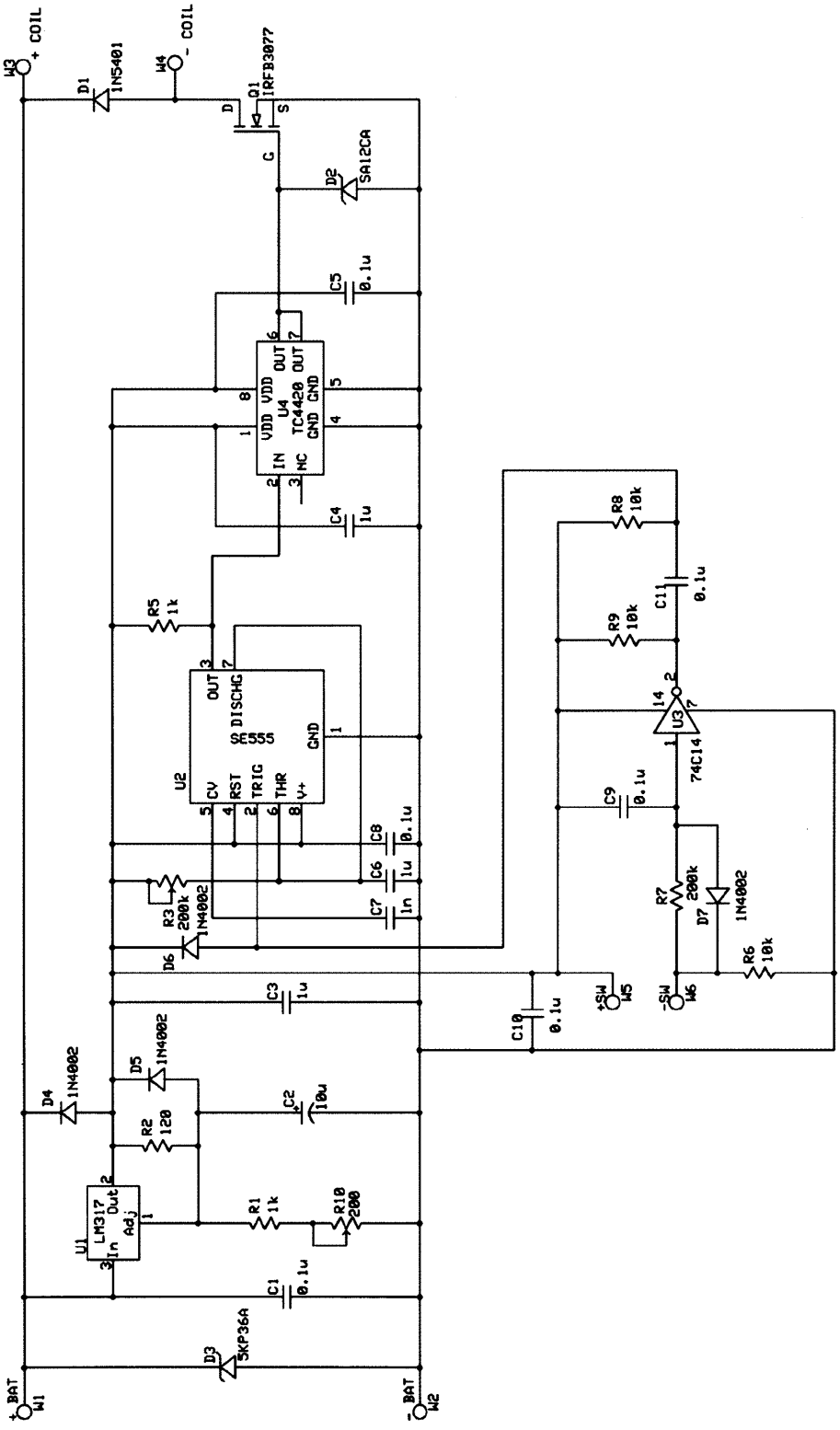

Figure 3-2: Electronic layout of the timer circuit.

cure to form a hole approximately 150 μm in diameter. The nozzle was then fitted into a compression fitting to connect to the solenoid valve.

In addition to the ease of use and ability to rapid-prototype, one advantage to a nozzle fabricated by stereolithography was its optical clarity, which permitted one to qualitatively observe the powder (e.g. for powder clogging) by visual confirmation. A second advantage was the the lower elastic modulus of the cured resin (when compared to metal). When strain gauges were installed to infer the internal pressure of the nozzle during injection (Section 4.1.1), a lower amplification of the voltage output was therefore required (compared to what would be necessary for a metal nozzle) thus leading to a higher signal to noise ratio.

One of the difficulties associated with fabricating nozzles in this manner was the requirement that minuten pins be manually inserted through 2 mm of resin; during this process these pins often bent and permanently deformed in the middle of the insertion. It was also deemed impractical to use thinner pins to fabricate nozzles of smaller diameter orifices. Furthermore, it was found by experimentation that orifice diameters expanded with each injection due to the erosion of the orifice by the injectable and deformation under pressure.

3.6.2 Composite Nozzle

Because of the fabrication difficulties and limited use of nozzles fabricated via stereolithography, a method to rapidly prototype nozzle orifices of different diameters was developed. By modifying the power and cut parameters of a laser machine, acrylic disks having a range of different sized holes could be quickly fabricated.

A carbon steel compression fitting (Parker Yor-Lok) was used to house one acrylic disk and a machined aluminum piece was used to mate to the surface of the inside of the compression fitting (Figure 3-4). When the pieces were assembled and tightened in the compression fitting, the acrylic disk and aluminum piece were compressed together to form a gas-tight seal in the fitting (Figure 3-5), resulting in a composite nozzle that could house acrylic disks of different orifice geometries. Acrylic, 1.7 mm thick, was laser machined to yield orifice diameters ranging from 20 to 200 μm (Figure

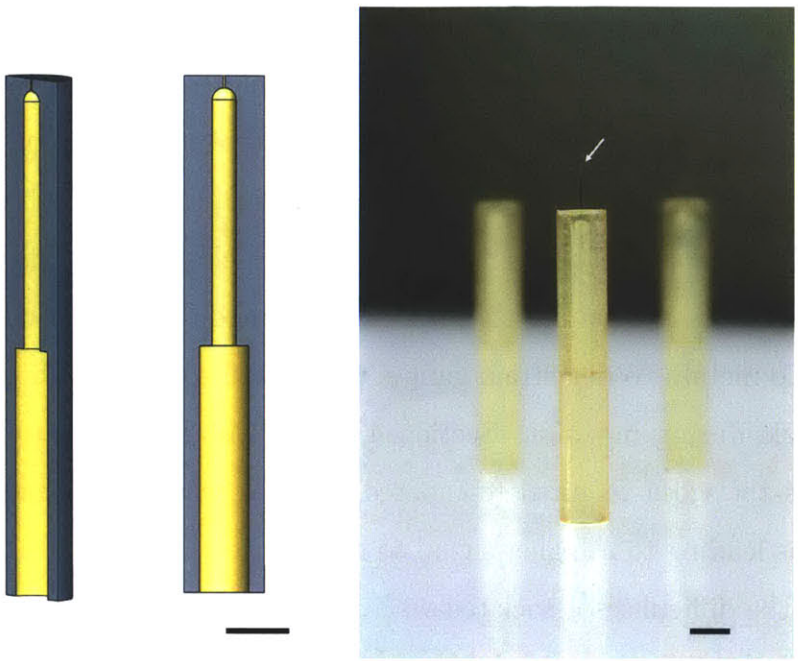

Figure 3-3: A CAD drawing and picture of the SLA produced nozzle. In the nozzle in the foreground of the picture, the minuten pin has not yet been removed and can be seen (scale bars = 5 mm).

3-6).

While the ability to rapidly prototype a range of orifice diameters was advantageous for experiments that varied jet power, the disadvantages eventually outweighed the advantages. First, because the laser machine was only accurate to within 30 μm, many acrylic disks had to be fabricated before obtaining a disk with the desired orifice diameter. Secondly, orifices of smaller diameters were tapered more than those of larger diameters. This variation of 3D geometry was an uncontrollable variable that may have affected the behavior of the fluid flow in the nozzle. The gravest issue however was the increase in orifice diameter during injection due to plastic deformation under pressure and abrasion by the injectable. Orifice diameters often expanded more than 40 μm during a single injection and therefore represented an uncontrollable variable in experimentation.

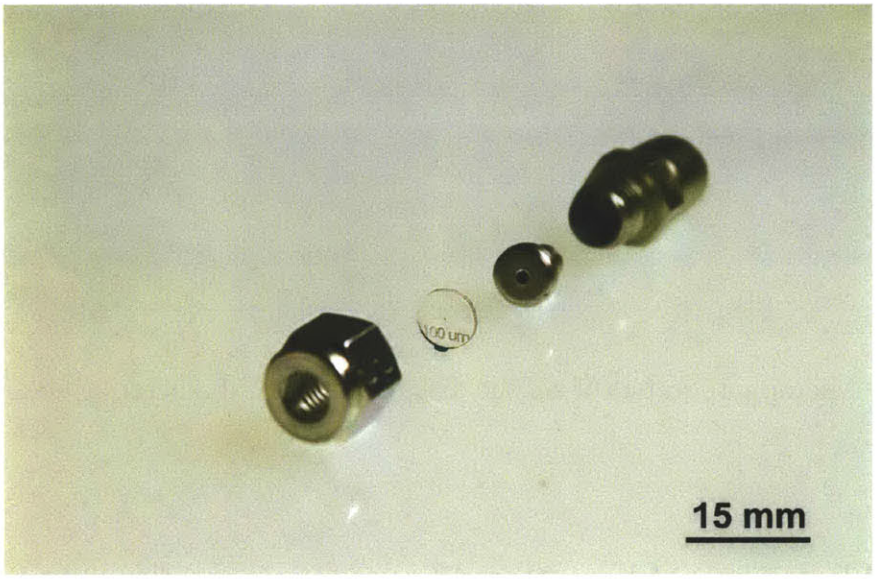

Figure 3-4: The outer housing of the compression fitting houses an acrylic disk and a custom-machined aluminum piece to mate to the compression fitting surface.

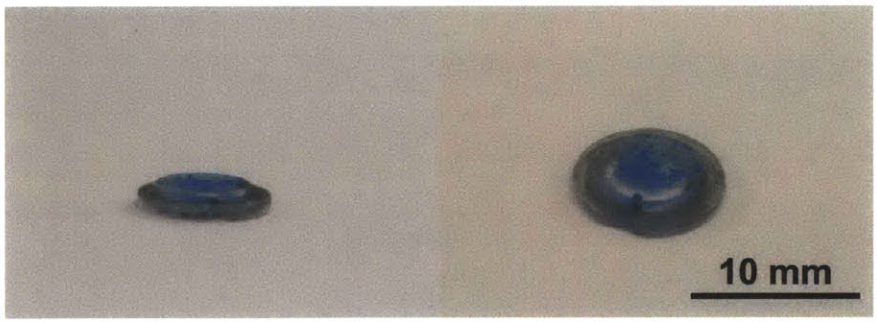

Figure 3-5: Compressed acrylic disks act as rigid o-rings to seal the composite nozzle. The observable blue color on top of the disk is the residual powder that remains on top of the disk after injection.

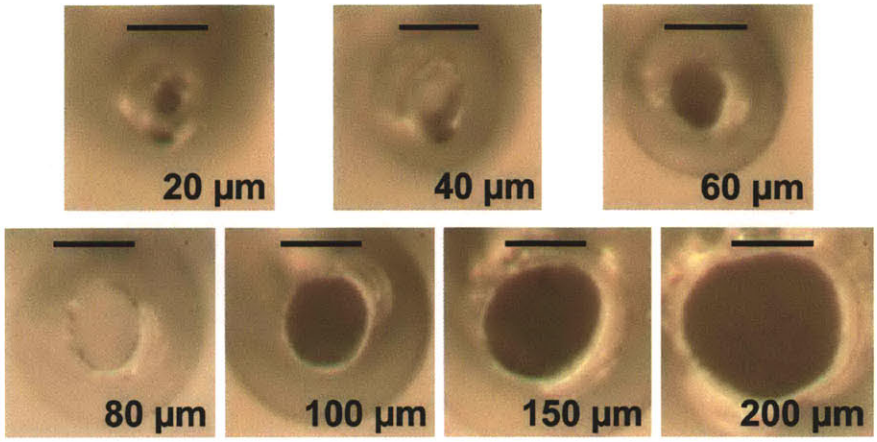

Figure 3-6: Microphotographs of acrylic disks of different diameter orifices (scale bars = 100 μm).

3.6.3 Aluminum Alloy Nozzle

To ensure a constant orifice diameter during the injection, a one-piece nozzle was designed and machined out of 7075 Aluminum alloy (Figure 3-7). This alloy was chosen for its high yield strength. To achieve a range of diameters, the nozzle was micro-drilled using drills of diameters 50, 75, 100, 125, 150, 175, and 200 μm, yielding nozzles with orifice diameters of 61, 81, 107, 136, 162, 197, 195 μm. Orifice diameters were measured by observation under the microscope.

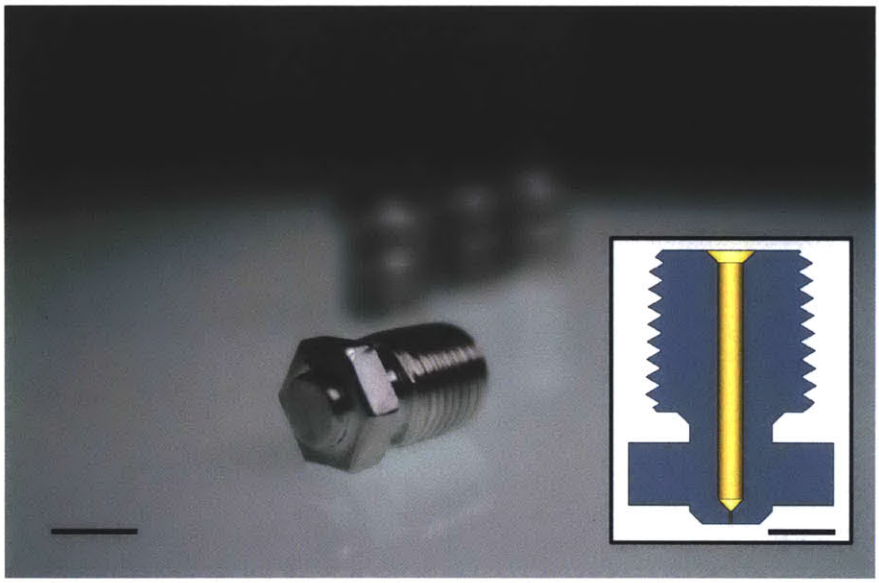

Figure 3-7: The 7075 aluminum alloy nozzle. Scale bars in the picture and its inset are 10 mm and 5 mm, respectively.

Chapter 4

Device Characterization

Three main metrics were chosen to characterize the needle-free gas-powered injector: the internal pressure the nozzle experiences during an injection, the speed of the powder as it leaves the nozzle, and the volume of gas delivered per injection.

4.1 Profile of the Pressure in the Nozzle

To measure the profile of the pressure in the nozzle, strain gauge measurements were performed to infer the internal pressure in the nozzle. These measurements were then reconciled with theoretical predictions.

4.1.1 Strain Gauge Measurements

In order to obtain optimal strain gauge measurements, stereolithography (SLA) produced nozzles were chosen. The cured resin formed by SLA has a lower Young's modulus than aluminum, which yields a larger strain per unit of induced stress. Two strain gauges were installed on the SLA-produced nozzle (Figure 4-1): one having its main axis along the nozzle's circumference and the other having its main axis along the length of the nozzle. These two strain gauges were placed in a dual wheatstone bridge configuration to minimize thermal effects of the strain gauges. The voltage measurements were calibrated to pressure values by sealing the nozzle from the sur-

roundings, opening the valve directly to the gas regulator and comparing the voltage output of the strain gauges to the measurements of the pressure sensor at different values of applied pressure.

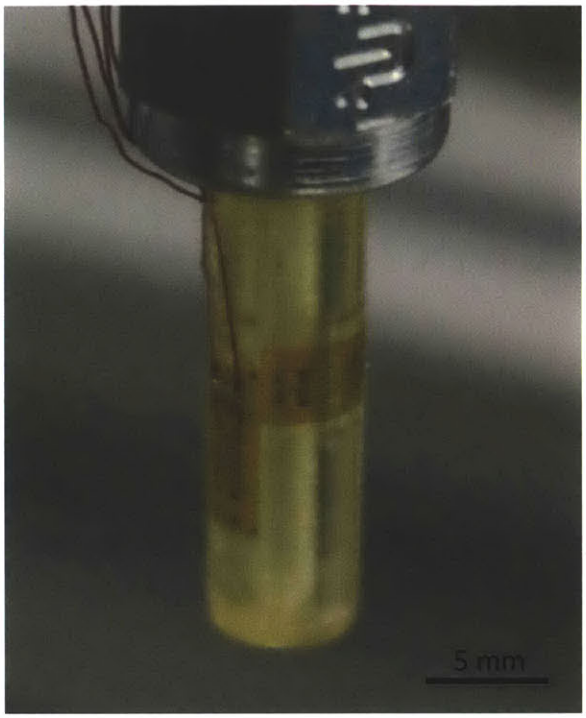

Figure 4-1: Two strain gauges are installed perpendicular to each other to infer the pressure inside the nozzle.

Figure 4-2 shows the pressure profiles of the nozzle (with no load) with a valve opening time of 15 ms at varying applied pressures: 2.5, 5.0, 7.5, 10.0, and 12.5 MPa.

4.1.2 Theoretical Prediction of Pressure Decay

The Bird, Stewart, Lightfoot (BSL) source-term model [27] predicts choked gas flows from a pressurized gas system:

$$t = [F(t)^{(1-\gamma)/2} - 1](\frac{2}{\gamma - 1})(\frac{V}{CA})[\frac{g_c \gamma P_0}{d_0}(\frac{2}{\gamma + 1})^{(\gamma+1)/(\gamma-1)}]^{-\frac{1}{2}}, \tag{4.1}$$

where:

- t = time after leak flow starts

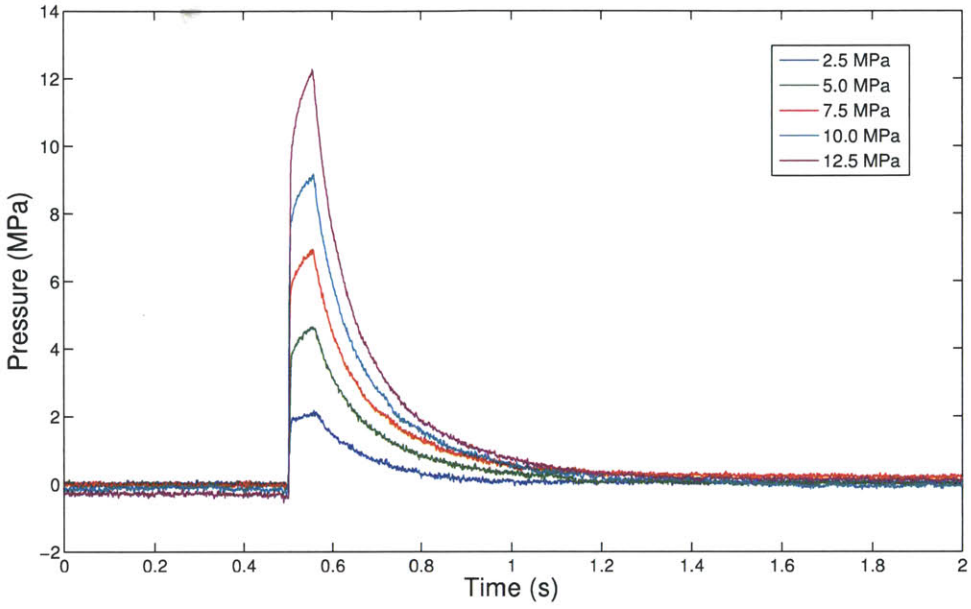

Figure 4-2: Pressure profile of the nozzle at varying applied pressures: 2.5, 5.0, 7.5, 10.0, and 12.5 MPa.

- F(t) = fraction of initial gas weight remaining in source vessel at time t
- V = volume of the source vessel
- C = coefficient of discharge, (0.60)
- A = area of the source leak
- γ = the adiabatic constant, c_p/c_v
- g_c = gravitational conversion factor
- P_0 = initial gas pressure in source vessel
- d_0 = initial gas density in source vessel

The isentropic expansion of an ideal gas is described by,

$$P(F) = P_0 F(t)^{\gamma}. \tag{4.2}$$

Then rearranging Equations 4.1 and 4.2 we obtain an expression for P(t):

$$P(t) = P_0[\frac{1}{a}t + 1]^{\frac{2\gamma}{1-\gamma}}, \tag{4.3}$$

where,

$$a = (\frac{2}{\gamma - 1})(\frac{V}{CA})[\frac{g_c \gamma P_0}{d_0}(\frac{2}{\gamma + 1})^{(\gamma+1)/(\gamma-1)}]^{-\frac{1}{2}}. \tag{4.4}$$

Making the assumption that the nozzle is completely filled with gas stored at the peak pressure until an opening at t = 0, we use the BSL source model to make a theoretical prediction of the decay of pressure in the nozzle and compare it with the experimental data of the decay of a 5 MPa ejection (Figure 4-3). We see that the theoretical prediction agrees well with experimental results. Therefore, choked flow accurately describe the behavior of the gas flow of an ejection.

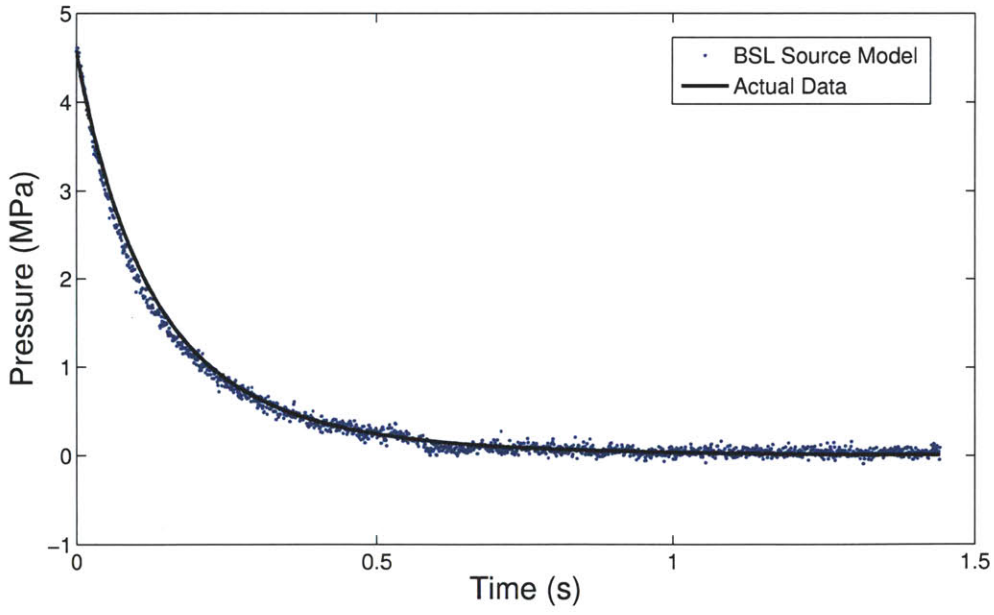

Figure 4-3: Pressure decay in the nozzle of a 5 MPa ejection due to gas escaping the nozzle.

4.2 Velocity of Injection

4.2.1 High Speed Camera Measurements

To determine the speed of an ejection, a series of ejections into air were recorded using a high-speed CMOS video camera (Phantom v9, Vision Research [28]) fitted with a 65 mm macro photo lens (Canon MP-E 65). The ejections were captured at a resolution of 1440 × 720 and a frame rate of 6420 fps. The pressure of ejection was 10 MPa and the speed of the front of the powder jet when already diverged was 12.13 m/s.

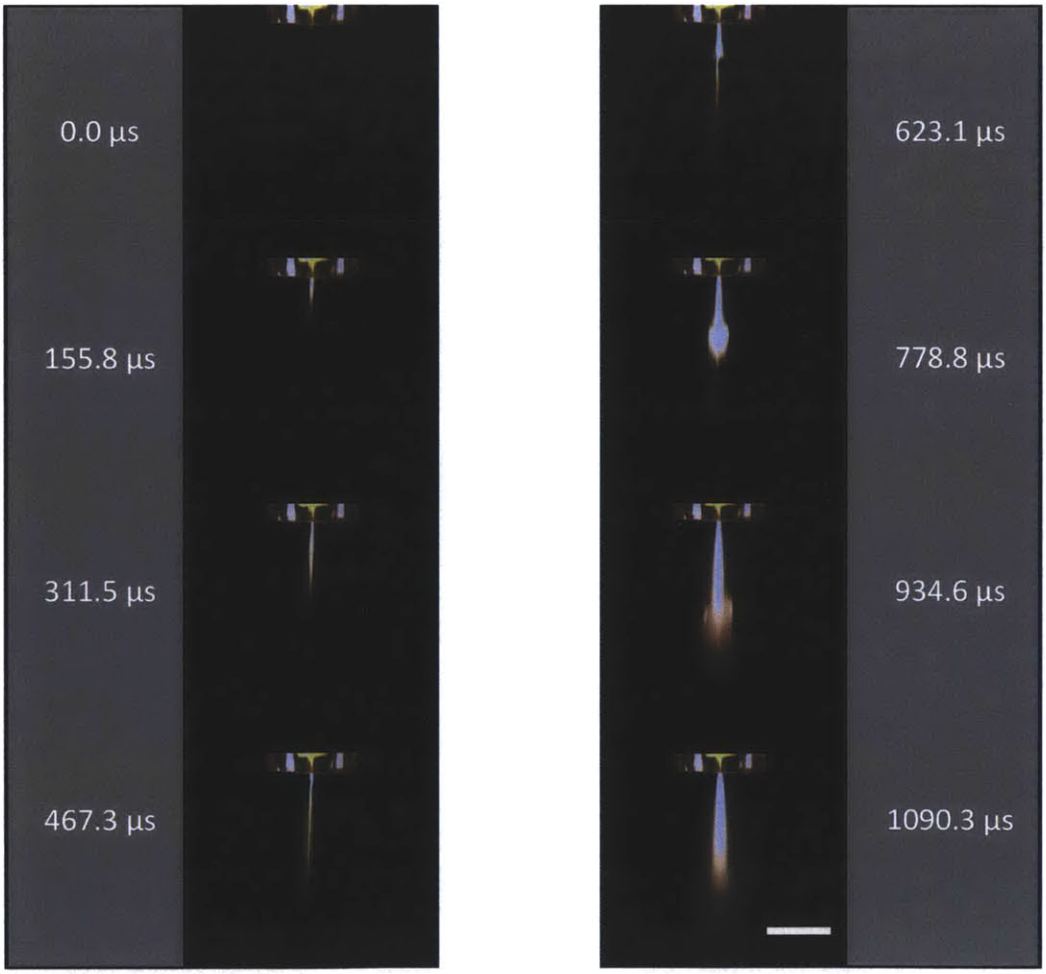

Figure 4-4: 6420 fps, 155.8 μs exposure, leading edge: 9.367 m/s, following plume: 12.130 m/s (scale bar = 5 mm).

4.3 Volume of Gas Injected

To determine the volume of gas injected in a single trial, the nozzle setup was placed in a sealed Buchner flask, and the difference in pressure within the chamber before and after an injection trial was measured using a pressure sensor (Vernier GPS-BTA) (Figure 4-5). The volume of helium delivered in a porcine tissue injection was found to increase with pressure, from 4.9 mL at 2.1 MPa to 10.4 mL at 10.2 MPa (Figure 4-6). Comparison of injections into tissue to control ejections into air demonstrates that the presence of a load greatly decreases the volume of gas delivered.

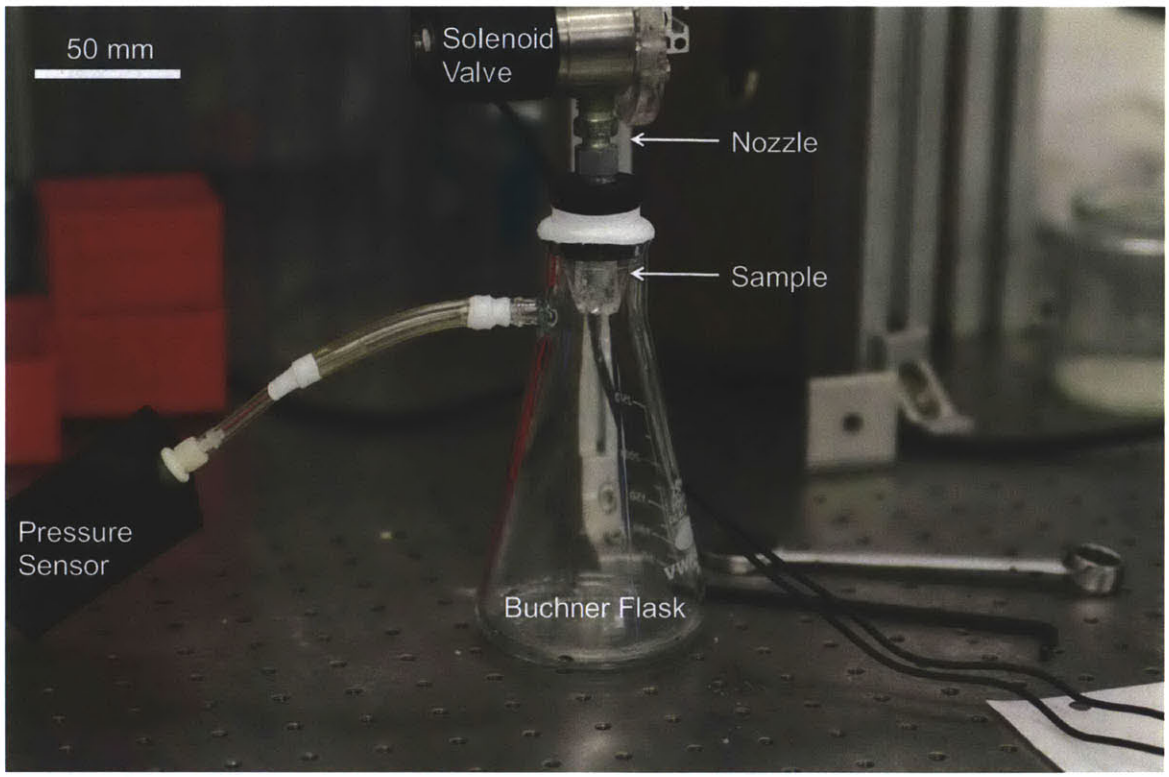

Figure 4-5: Setup to measure volume of gas ejected.

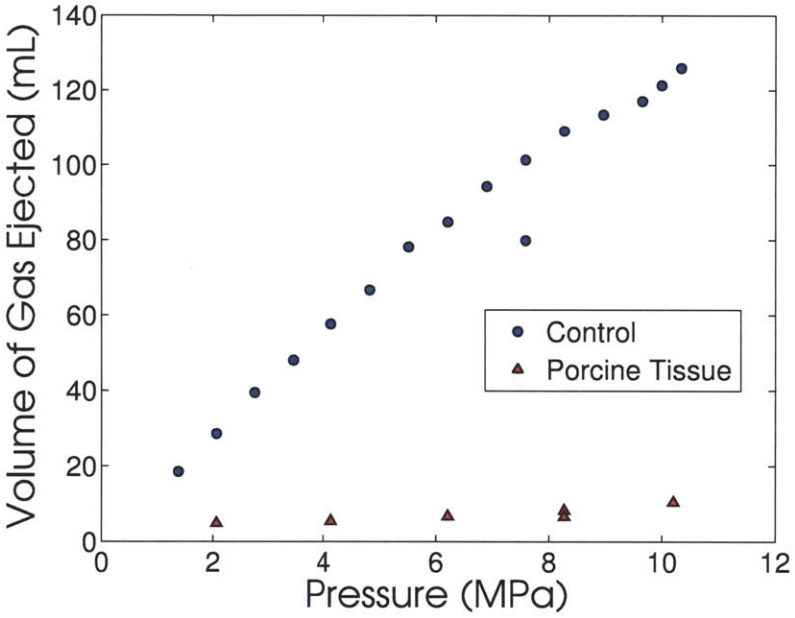

Figure 4-6: Volume of gas injected from the nozzle (mL) as a function of applied pressure (MPa). Ejections into air served as the control.

Chapter 5

In Vitro Injection Experiments

Design verification was carried out by performing injections into porcine tissue, a close analog to human tissue.

5.1 Experimental Procedures

Post mortem porcine tissue was obtained through the MIT Tissue Harvest Program using procedures approved by the IUCAC and in accordance with the NIH Guide for the Use and Care of Laboratory Animals. Tissue was harvested from the abdomen of Yorkshire pigs (approximately 6 months in age) immediately after euthanasia and included muscle, subcutaneous fat, and skin. The tissue was trimmed, immediately vacuum sealed, and stored at -80 °C. Prior to injection, each sample was thawed at 4 °C and equilibrated to room temperature. All injections were done by placing the nozzle in direct contact with the tissue sample. Injected tissue was placed in plastic containers (22 mm × 22 mm × 18 mm) containing optimal cutting temperature compound (Tissue-Tek OCT Compound) and frozen in liquid nitrogen. Tissue slices, 15 μm thick, were then successively removed from each sample using a Vibratome Ultra Pro 5000 cryostat. A Canon EOS-7D camera, fitted with a 65 mm macro photo lens (Canon MP-E 65) was used to photograph the tissue after removal of each section, yielding a series of photographs that when compiled, imaged through the entire block of tissue. To view the different layers of porcine tissue, tissue was embedded in OCT

and microtomed using the cryostat to yield 20 μm sections, which were captured on microscope slides. These sections were consequently fixed in cold acetone and stained with Mayers hematoxylin.

5.2 Successful and Unsuccessful Injections

The jet once it has punctured the stratum corneum may produce two effects. In the first case, an erosion hole is created but powder is not dispersed through the tissue (Figure 5-1a) while in the second case, an erosion hole is created followed by dispersion of drug into the tissue (Figure 5-1b). These two cases were carefully differentiated by visual assessment. When an erosion hole is created without powder dispersion, the powder resides only on the exposed surface of the erosion hole. For the purpose of analysis, an injection yielding an erosion hole with no powder dispersion is not considered to represent a successful injection. As such injection profiles have been quantified using two measurements: D_h the depth of the erosion hole and D_d the depth of powder dispersion.

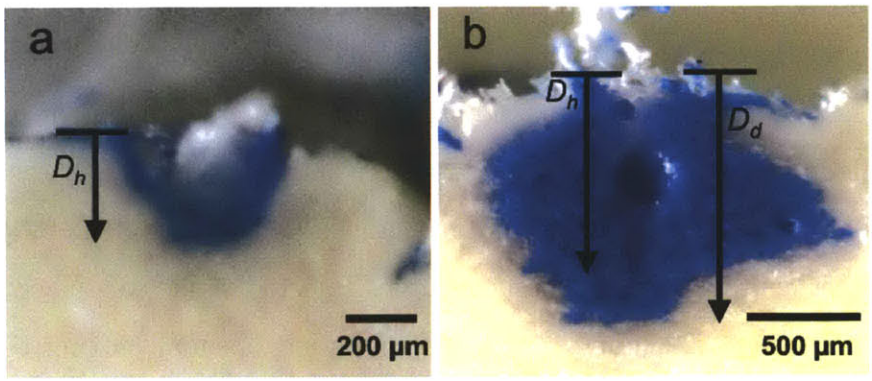

Figure 5-1: Representative tissue midline cross-sections of two types of injection trials: (a) an erosion hole with no dispersion in tissue which is considered unsuccessful and (b) an erosion hole with powder dispersion considered to be successful. Frozen OCT in the erosion hole has a bluish white appearance. In (b) an air bubble in the frozen OCT appears as a darkened hole in the middle of the erosion hole.

5.3 Inflation of Tissue during Injection

In successful injections, it was often observed that the helium inflated the tissue sample. Figure 5-2 shows a time-lapse series of photographs demonstrating tissue inflation at 0.05 s after the start of injection and deflation within 1.22 s. The observation of tissue deflation and the observation that the vast majority of powder injections are delivered to the upper region of the dermal layer (Section 5.6) (where major arteries and veins are not located), are consistent with the conjecture that injection of helium into the upper layers of tissue poses minimal health risk (Section 3.3). Still, deflation could primarily be attributed to gas escaping through the fat layers of the sides of the tissue sample, a mode of escape that would be unavailable in an *in vivo* injection. Further experiments would need to be carried out to verify whether gas deflation still occurs when its only mode of escape is diffusion back through the skin layer.

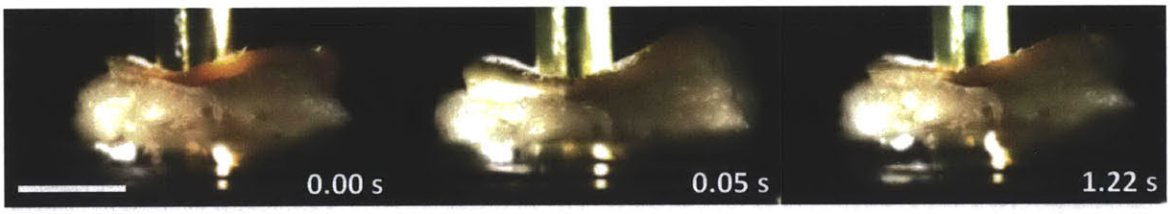

Figure 5-2: Time-lapse photograph series of pre-, mid-, and post-injection using the SLA produced nozzle. Note the inflation in the second picture (0.05 s) and deflation in the third (1.22 s) (scale bar = 10 mm).

5.4 Quantity of Powder Delivered

Percent yield of delivery is an important metric when assessing the efficacy of an injection method. While mass measurement before and after injection is a common method used in liquid injections to determine the volume of drug injected into the tissue, this was found to be an impractical method for powder injections. In one or two minutes, a piece of freshly exposed tissue (approximately 20 mm $\times$ 20 mm in area) loses 2 to 5 mg of mass due to dehydration (Figure 5-3). Since the powder loaded into

the nozzle per injection is on the order of 1 mg (as opposed to approximately 25–200 mg for liquid injections) a mass measurement yields no usable information. Future work would entail employing techniques such as measuring the levels of fluorescence or radioactivity of the tissue after delivery of fluorescent or radioactive particles, respectively.

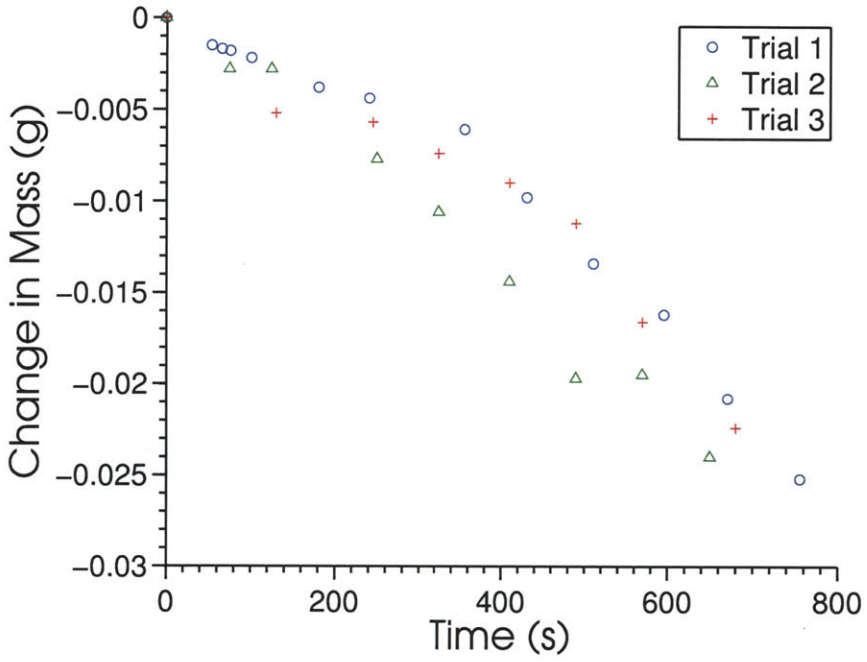

Figure 5-3: Change of tissue mass (g) due to dehydration at ambient humidity and temperature. The mass of these tissue samples used for dehydration experiments were comparable to tissue samples used for injection experiments.

5.5 Dispersion Pattern in Tissue

Image processing and 3D reconstruction of the injection were performed in MATLAB [29] (Appendix A) to determine the dispersion pattern of each tissue injection. Image thresholding was performed on each picture according to its hue, saturation, and luminance value (hsv) and a border was defined around the remaining area after superposition (Figure 5-4). Each picture's border of the powder in the tissue was then successively 3D plotted to its corresponding depth on the z-axis. Finally, a

surface was defined around the series of borders to yield the 3D dispersion pattern of the powder injection.

Reconstruction of successful powder injections into porcine tissue revealed that the dispersion patterns were quite varied. The most common shapes observed in successful injections could be classified as an upside down cone (Figure 5-5a), an upright cone (Figure 5-5b), or a sphere (Figure 5-5c).

These injection shapes are associated with the development of the actual injection. An upside down cone was observed with the most shallow of injections, whereas the sphere was commonly observed with the deepest of injections. Fluid and powder dispersion within tissue originates from what can be thought of as a point source of radially outward flowing fluid [14]. As dispersion depth increases, the point source also increases in depth and a greater section of the sphere is realized; in a shallow injection, this point source can be thought of as resting on the surface, hence only the bottom part of the sphere is realized. The intermediate stage between the upside cone and sphere may be thought of as an underdeveloped sphere, and thus the shape more closely resembles a right side cone. These observations are similar to those for needle-free injections using aqueous solutions and are consistent with the point-source hypothesis for incompressible fluid injection. A deeper understanding of the tissue mechanics that predict dispersion pattern could be beneficial to further optimize delivery of drugs to specific depths in the tissue.

5.6 Depth of Injection

To test the controllability of the device, two parameters of jet power, nozzle orifice diameter and applied pressure, were varied to observe the consequent depth of injection. Depth of injection was determined by measurement after medial section or 3D reconstruction of the dispersion pattern. In addition, the specific layer of tissue that powder had been delivered to was inferred by comparison with a representative tissue section counterstained with Mayers hematoxylin. A typical section of tissue stained with Mayers hematoxylin is shown in Figure 5-6 and shows a dermal layer 2.5 mm

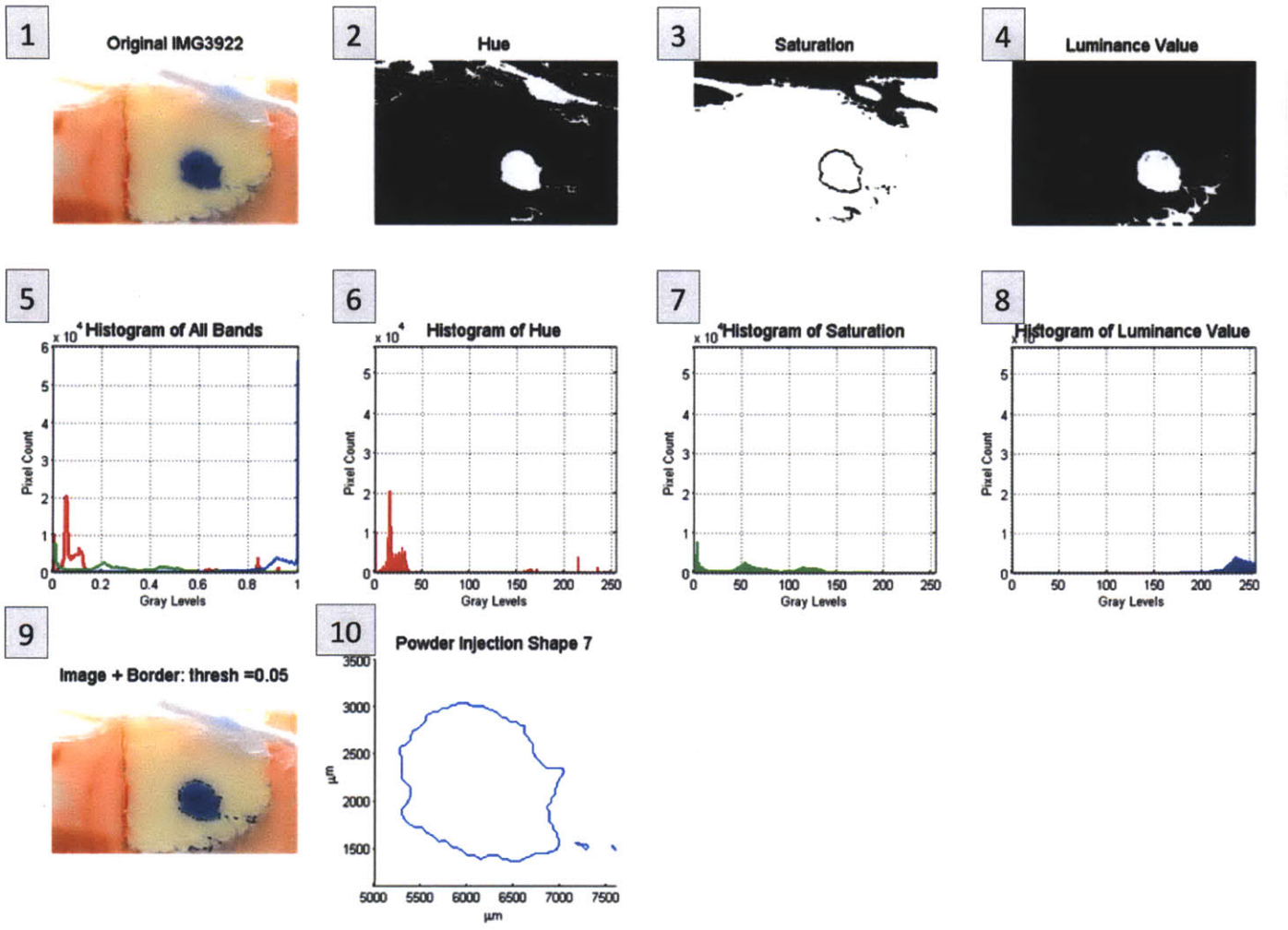

e 5-4: The figure output of a MATLAB script assists the user in determining the appropriate hsv values by defin r around the superposition of thresholded hue, saturation, and luminance images according to a hsv value that the s. The image displays: 1) the original image, 2–4) each image after thresholding according to a given hue, saturatic ance value, 5–8) histograms of the hue, saturation, luminance, 9) a superposition of the image and the defined bc 0) an isolated plot of the defined border.

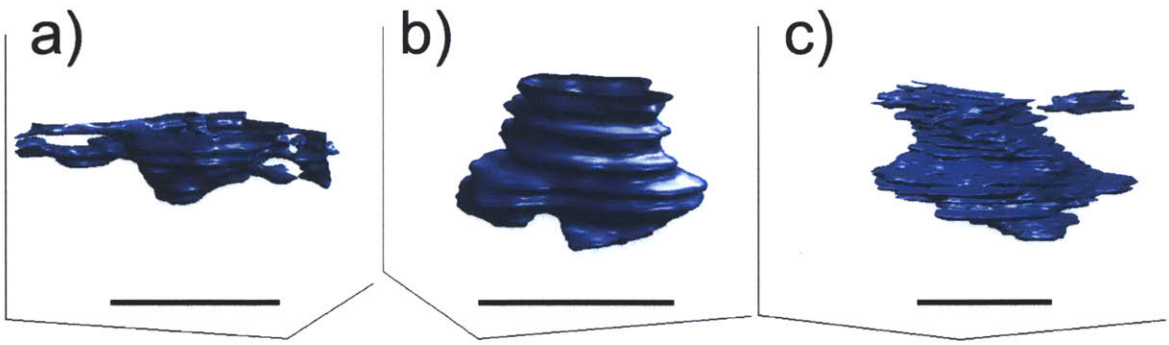

Figure 5-5: 3D MATLAB reconstructions of the tissue injection shape. Three primary shapes were observed (a) upside down cone, (b) right side cone, and (c) sphere. The powder dispersion depth corresponding to each shown 3D reconstruction is 441, 810, and 1125 μm, respectively (scale bars = 1 mm).

thick and a fat layer that is at least 3 mm thick.

5.6.1 Diameter Dependence Trials

Because the composite nozzle (Section 3.6.2) could easily house acrylic disks having orifices of a range of diameters, it was used to perform injections to determine the effect of varying orifice diameters on injection depth. Three sets of trials at different applied pressures were performed: 8.9–9.0 MPa, 10.1 MPa, and 13.7–13.8 MPa. The depths of erosion hole and dispersion of these single trials are plotted in Figure 5-7 and Figure 5-8, respectively. Given the expansion of the orifice during injection, the average of orifice diameters before and after injection is presented on the x-axis. Injection success and failure is also differentiated in each data set. The ranges of nozzle orifice diameters, depths of erosion hole, and depths of dispersion are summarized in Table 5.1. In general, we observed a correlation of both erosion hole depth and dispersion depth with increasing orifice diameter.

To observe more clearly the correlation of both erosion hole depth and dispersion depth with nozzle diameter, the data was grouped into 25 μm ranges (n = 2–4) and the respective depths were averaged (Figure 5-9).

For an applied pressure of 8.9–9.0 MPa, trials were unsuccessful in the 25–75

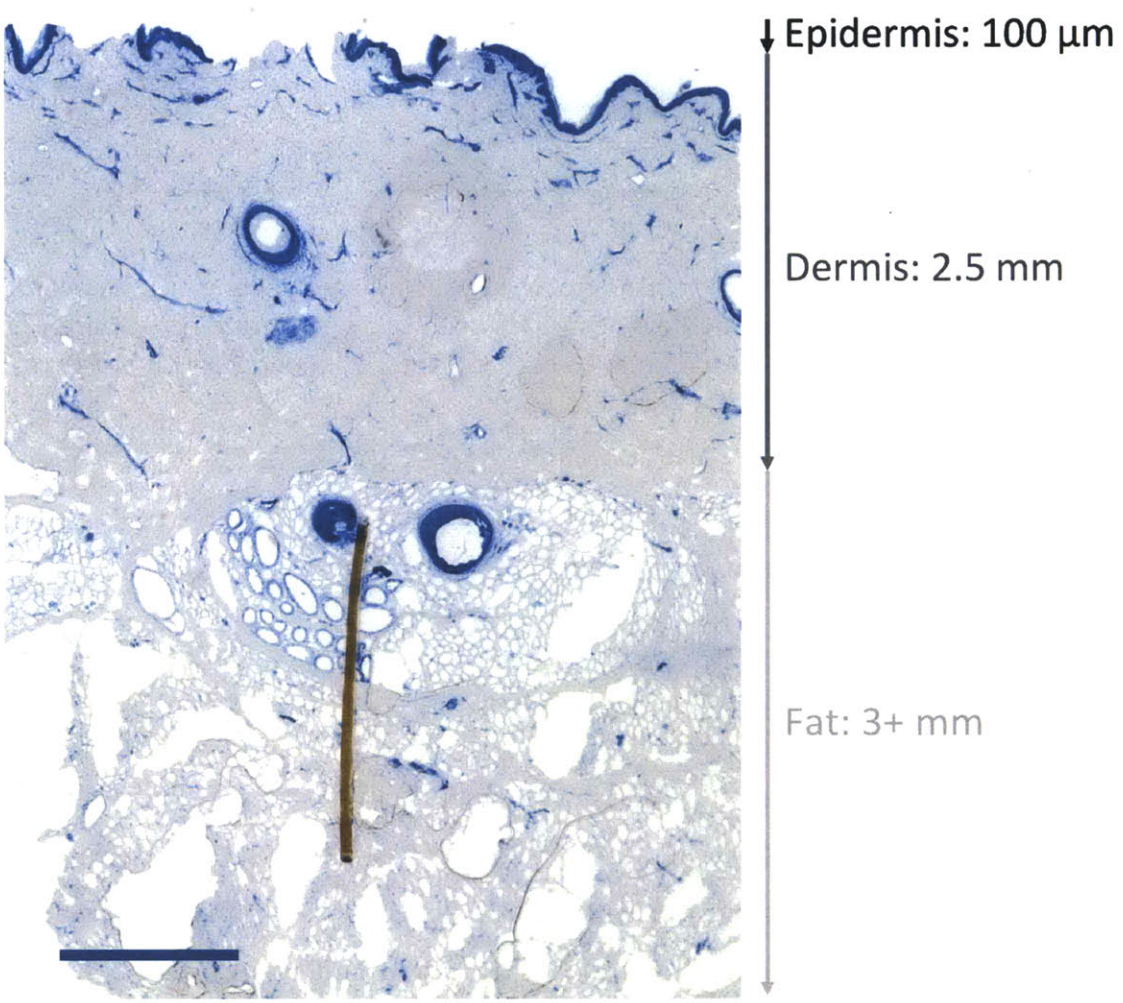

Figure 5-6: Photograph of a representative 20 μm section of porcine tissue stained with Mayers hematoxylin (scale bar = 1 mm).

Set	Pressure (MPa)	Range of Orifice Diameters (μm)	Range of D_h (μm)	Range of D_d (μm)
1	8.9 – 9.0	33 – 173	91 – 860	260 – 1090
2	10.1	54 – 159	313 – 585	441 – 1125
3	13.7 – 13.8	74 – 265	210 – 1890	585 – 5310

Table 5.1: Compilation of the ranges of orifice diameters, D_h, and D_d for Sets 1–3.

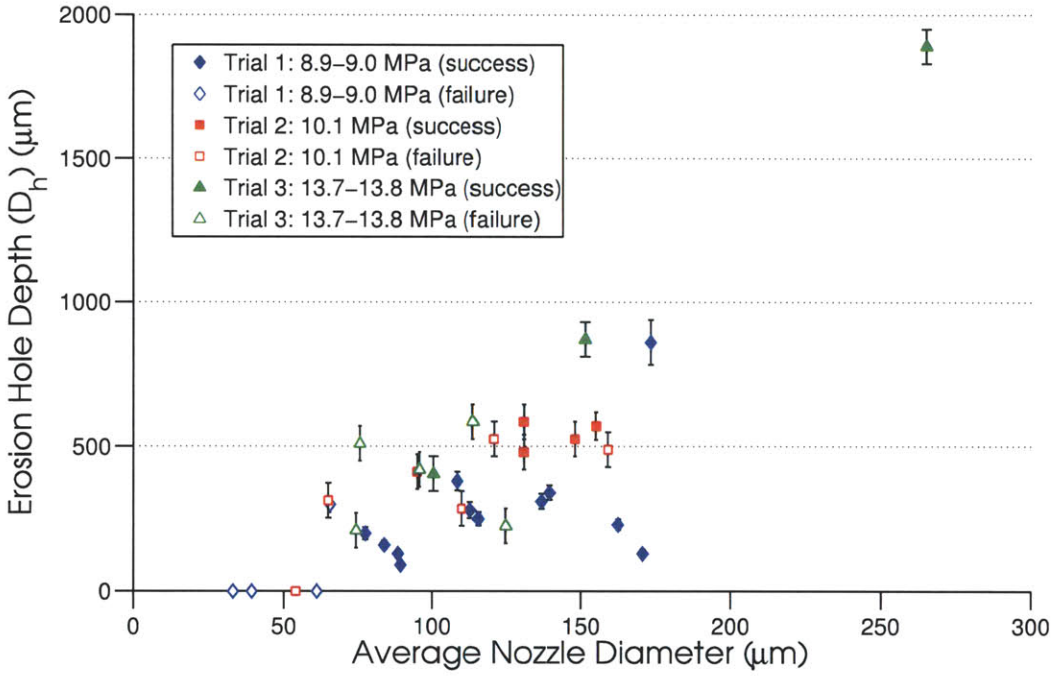

Figure 5-7: Dependence of D_h on average nozzle diameter at constant pressure. Solid markers represent successful injections, while open markers represent unsuccessful injections.

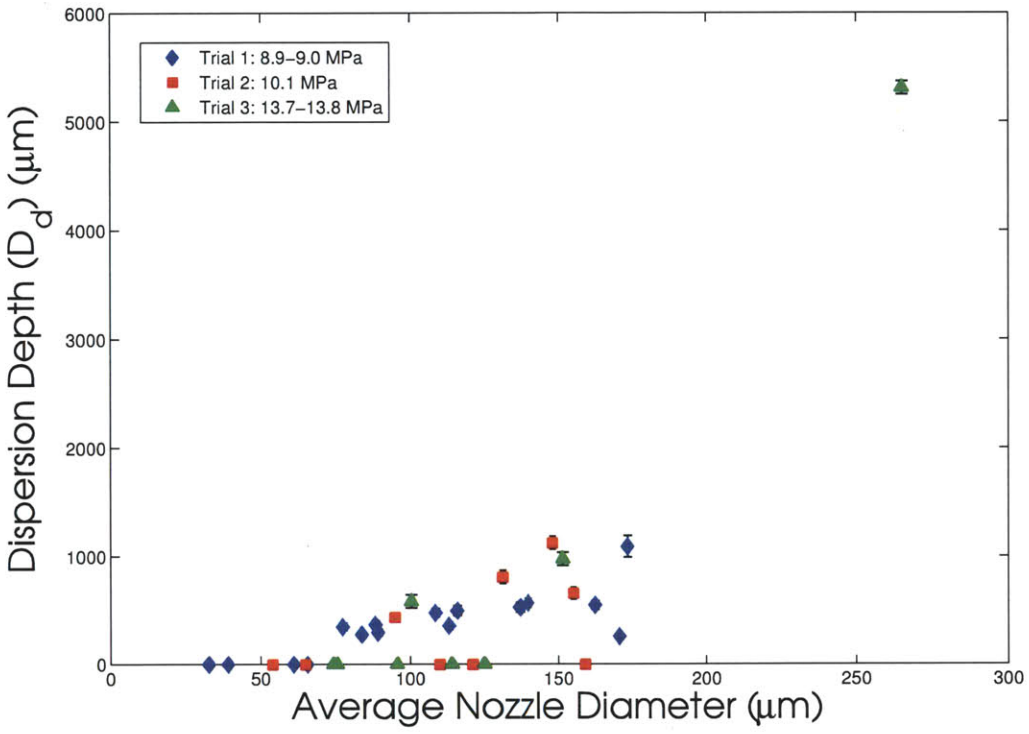

Figure 5-8: Dependence of D_d on average nozzle diameter at constant pressure. The injection depth of an unsuccessful injection is considered to be zero ($D_d = 0$).

μm range: erosion holes and powder dispersion were not observed in the 25–50 μm diameter range and erosion holes but not powder dispersion were observed in the 50–75 μm range. Both erosion holes and powder dispersion were observed (successful) in the 75–175 μm range.

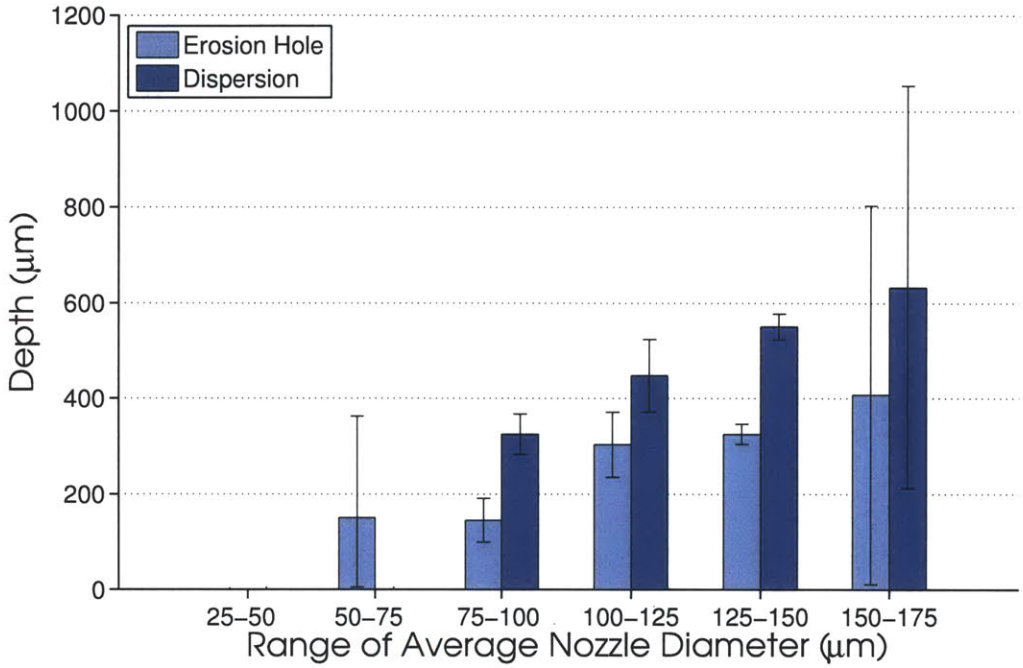

Figure 5-9: Depth data for 25 μm ranges of average orifice diameters at injections at 8.9–9.0 MPa of applied pressure. Depth of both erosion hole and powder dispersion generally increases with applied pressure.

Thus we see more clearly the trend of increasing erosion hole depth and dispersion depth with increasing nozzle orifice diameter.

The inherent limitation in interpreting the results of the experiments performed using the composite nozzle lies in the expansion of the orifice during an injection. Orifice expansion was generally in the range of 20–60 μm depending on the initial nozzle diameter and pressure setting. Across all trials, the average expansion during an injection was 47 μm. Because the time progression of the orifice expansion during an injection is unknown, the actual diameter of the powder jet the tissue is experiencing at a given point in time during an injection is also unknown. This lack

of knowledge leads to an inability to make any statement on the injection depth's dependence on nozzle orifice diameter beyond correlation.

5.6.2 Pressure Dependence Trials

Because the orifice diameter of a composite nozzle was not fixed, an aluminum alloy nozzle (Section 3.6.3) was chosen to evaluate the relationship between injection depth and applied pressure. Injections were performed using a nozzle having a fixed orifice diameter of 136 μm at five different pressure settings: 2.5, 5.0, 7.5, 10.0, and 12.3 MPa.

At least one injection failed at every pressure setting in this set of experiments. We decide to address the success rate of injection separately (Section 5.7) and select only successful trials to plot the average dispersion depths (Figure 5-10).

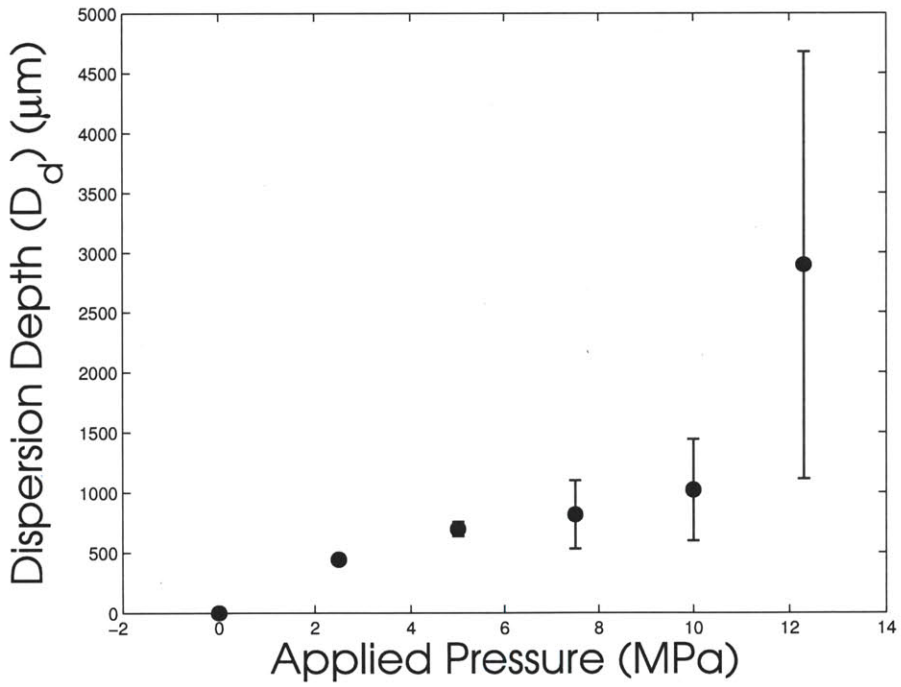

Figure 5-10: Dispersion depth versus pressure for successful injections. Each plotted point represents the average of a set of successful injection experiments (n = 1–3) at given pressure settings: 2.5, 5.0, 7.5, 10.0, and 12.3 MPa.

We observe a trend of increasing dispersion depth with increasing pressure, consistent with the previously stated theory of jet power.

5.6.3 Jet Power Dependence

To compare together all sets of *in vitro* injection trials presented in this thesis, we would like to use jet power (see Section 2.3.1) as a metric. As this variable includes jet parameters of both applied pressure and orifice diameter, it is appropriate then to combine the sets of diameter dependence trials (Section 5.6.1) with the set of pressure dependence trial (Section 5.6.2).

There are two challenges in calculating the jet power of a jet composed of gas and powder.

First, given the observation that the tissue sample inflates and deflates during injection (Section 5.3), we know then that the internal pressure of the tissue will be greater than atmospheric pressure during the injection, but we do not know how much greater the pressure will be without experimental measurement. Thus we do not know whether the criteria for choked flow (Equation 2.4) holds during the duration of the injection and Equation 2.12 may therefore not be a proper expression for jet power during the injection. However, at the instant the injection begins, the tissue is still at atmospheric pressure, and therefore the initial flow can be characterized as choked. Thus, we can use initial jet power as a metric.

Secondly, it is currently unclear how the entrainment of powder affects the behavior of the jet. Powder entrainment in the gas jet could greatly increase the effective density of the jet. Given a peak pressure of 10 MPa, the exit density of a jet whose volume is composed of 0.5% powder would be more than double the density of an equivalent jet without powder. However, the inertia of powder a gas is able to impart likely increases with the inertia of that gas. If so, then the effective density of powder entrained in the gas would also increase with the exit density of the jet of gas. Then observed trends with calculations of jet power neglecting powder entrainment would still be consistent to calculations of jet power taking into account powder entrainment. Experimental work to measure the effective density of a jet composed of gas

and powder would be required to verify this hypothesis.

Having qualified the use of Equation 2.12 as an expression for the initial jet power of an injection, we plot the dispersion depth of all successful trials against the calculated initial jet power (Figure 5-11).

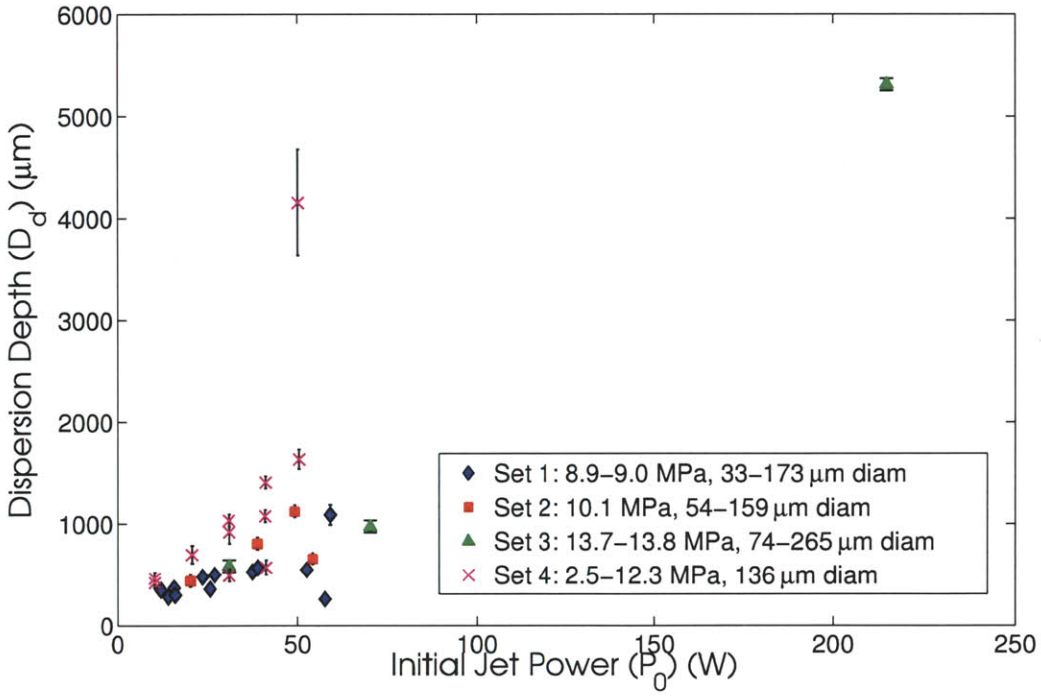

Figure 5-11: Dispersion depth versus initial jet power for all successful injection trials.

There is a general increase in dispersion depth with an increase in initial jet power. Given our knowledge of the thicknesses of each tissue layer (Figure 5-6) we note that all injections except for two have delivered powder to the dermis.

5.7 Success Rate of Injections

The data suggests that the success rate of an injection increases with increasing orifice diameter. A graphical representation of the success rates of injections using orifice diameters grouped by 50 μm ranges is shown in Figure 5-12.

The data also suggests that the success rate of injections is optimized by a certain value of pressure. We see that within both the 50–100 μm and 100–150 μm groups, the success rate of injection decreases with increasing pressure (pressure increases from the 8.9–9.0 MPa set to the 13.7–13.8 MPa set). In the 150–200 μm group, a similar relationship is observed between experiments performed at 8.9–9.0 and 10.1 MPa. The deviation from this trend at 13.7–13.8 MPa represents a single injection (n = 1) and as such may not be representative.

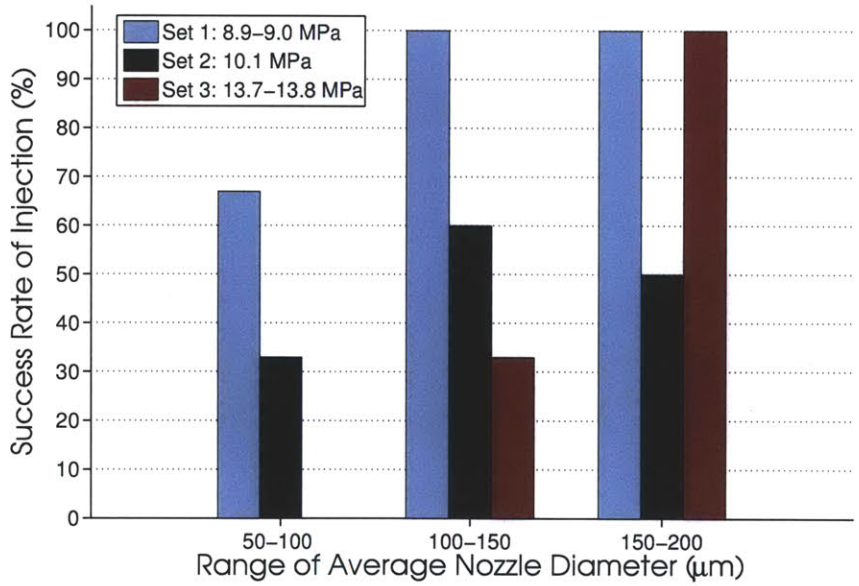

Figure 5-12: Success rate of injections of diameter dependence trials using the composite nozzle. Note that average nozzle diameters are presented because the expansion of orifices during injection. Data is grouped into 50 μm ranges (n = 1–6).

To further demonstrate the hypothesis that success rate is dependent on pressure, we plot the success rate of injections in pressure dependence trials in Figure 5-13. We note that the highest success rates are observed at P = 7.5 MPa and P = 10 MPa.

For the orifice diameter of 136 μm used in this set of trials, there seems to exist then an optimal pressure of injection between 7.5 and 10 MPa. This conjecture would also be consistent with the trend observed in Figure 5-12: within the 100–150 μm group there is a 100% success rate for the 9 MPa set which subsequently decreases to 33% for the 13.7–13.8 MPa set. The decrease of success rate for injections that use higher peak pressures is possibly due to the mass flow rate of the gas exceeding the maximum absorption rate of the tissue, forcing the gas to splash back out of the created hole instead of delivering the powder into the tissue. This "splash back" phenomenon has been observed in injections using aqueous solutions and can be improved by pressure pulse shaping [30].

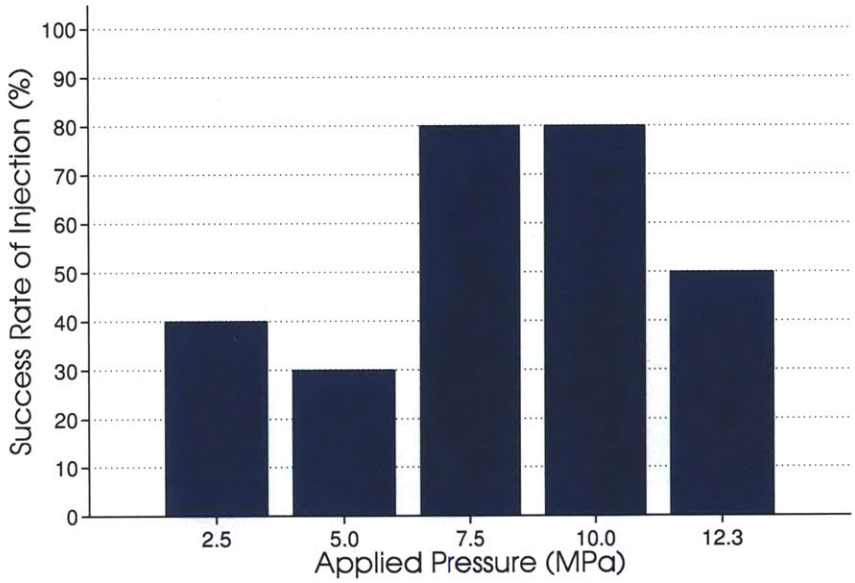

Figure 5-13: Success rate of injections of pressure dependence trials using a 136 μm diameter aluminum alloy nozzle (n = 4–5).

We thus conjecture that injection success rate increases with increasing orifice diameter and is optimized by a certain pressure value. The presented data suggests that a set of injection parameters that may optimize injection success rate is an orifice diameter of 150 μm and an applied pressure of 9 MPa.

Chapter 6

Conclusion and Future Work

6.1 Conclusion

A new method of powdered drug delivery has been developed and demonstrated. The developed device is a simple and inexpensive bench-top helium-powered device capable of delivering particles into porcine tissue to depths of 260 to 5000 μm. Because penetration of the powder is not dependent on ballistics but the jet mechanics of the carrying gas, penetration of particles of lower momentum density than has previously been attained is made possible.

The device presented offers an alternative method for the intradermal delivery of powdered drug and has the potential to be implemented with stabilized formulations of vaccines to address the cold chain problem. While the device uses a compressible fluid for jet injection, the penetration, success of injection, injection depth, and injection shape are consistent with previous results obtained using essentially incompressible fluids (aqueous solutions). It is shown that the depth of the powder's dispersion in the tissue is dependent on the jet power of injection, which can be varied by changing applied pressure or nozzle orifice diameter. It is conjectured that the success rate of injection could also be optimized by the jet parameters of applied pressure and nozzle orifice diameter. Further development of this type of technology could provide a platform for the delivery of a variety of powdered drug formulations and deliver to the subcutaneous and muscle layers of tissue.

6.2 Future Work

Future experimental work will include delivering thermo-stabilized formulations of vaccines, verifying their stability under high pressure and physical impact, and exploring parameters required for successful injections and bioavailability of the delivered drug.

Future device development will explore optimal nozzle geometries and development of a hand-held device, of which the design parameters are as follows:

1. be a handheld device
2. operate on battery power
3. be automatically reloading
4. use disposable nozzles
5. employ a controllable pressure waveform
6. be able to reliably inject drug to dermal, fat, and muscle layers of tissue

Bibliography

[1] M. Kane and H. Lasher. (2002) The case for childhood immunization. [Online]. Available: http://www.unicef.org/immunization/index_coverage.html 1.1

[2] T. L. P. Project. (2009) Progress toward immunization: Winning the fight against deadly diseases. [Online]. Available: http://www.gatesfoundation.org/livingproofproject/Documents/progress-towards-immunization.pdf 1.1

[3] W. B. WHO, UNICEF, "State of the world's vaccines and immunization," *WHO*, 2009. 1.1

[4] D. M. Matthias, J. Robertson, M. M. Garrison, S. Newland, and C. Nelson, "Freezing temperatures in the vaccine cold chain: A systematic literature review," *Vaccine*, vol. 25, no. 20, pp. 3980 – 3986, 2007. [Online]. Available: http://www.sciencedirect.com/science/article/pii/S0264410X07002289 1.1

[5] E. L. Giudice and J. D. Campbell, "Needle-free vaccine delivery," *Advanced Drug Delivery Reviews*, vol. 58, no. 1, pp. 68 – 89, 2006, challenges in Pediatric Drug Delivery: the Case of Vaccines. [Online]. Available: http://www.sciencedirect.com/science/article/pii/S0169409X0600007X 1.1, 1.2

[6] PATH. (2012) Not too hot, not too cold. [Online]. Available: http://www.path.org/projects/cold-chain.php 1.1

[7] D. Chen, S. Kapre, A. Goel, K. Suresh, S. Beri, J. Hickling, J. Jensen, M. Lal, J. Preaud, M. LaForce, and D. Kristensen, "Thermostable formulations of a hepatitis b vaccine and a meningitis a polysaccharide conjugate vaccine produced by a spray drying method," *Vaccine*, vol. 28, no. 31, pp. 5093 – 5099, 2010. [Online]. Available: http://www.sciencedirect.com/science/article/pii/S0264410X10006699 1.1

[8] S. Mitragotri, "Immunization without needles," *Nature Reviews Immunology*, vol. 5, no. 12, pp. 905–916, 12 2005. [Online]. Available: http://dx.doi.org/10.1038/nri1728 (document), 1.2, 1.2, 1-1

[9] S. S. Renteria, C. C. Clemens, and M. A. Croyle, "Development of a nasal adenovirus-based vaccine: Effect of concentration and formulation on adenovirus stability and infectious titer during actuation from two delivery devices." *Vaccine*, vol. 28, no. 9, pp. 2137–2148, Feb 2010. 1.2

[10] D. P. Wermeling, S. L. Banks, D. A. Hudson, H. S. Gill, J. Gupta, M. R. Prausnitz, and A. L. Stinchcomb, "Microneedles permit transdermal delivery of a skin-impermeant medication to humans," *Proceedings of the National Academy of Sciences*, vol. 105, no. 6, pp. 2058–2063, 2008. [Online]. Available: http://www.pnas.org/content/105/6/2058.abstract 1.2

[11] Bioject. (2012) Bioject website. [Online]. Available: www.bioject.com (document), 1.2, 1-2

[12] Injex. (2012) Injex website. [Online]. Available: www.injex.com (document), 1.2, 1-2

[13] A. Taberner, N. C. Hogan, and I. W. Hunter, "Needle-free jet injection using real-time controlled linear lorentz-force actuators," *Medical Engineering and Physics*, p. in press, 2012. [Online]. Available: http://www.sciencedirect.com/science/article/pii/S1350453311003249 (document), 1.2, 1-2

[14] I. A. Coalition. (2011) Vaccines with diluents: How to use them. [Online]. Available: http://www.immunize.org/catg.d/p3040.pdf 1.2

[15] T. L. Burkoth, B. J. Bellhouse, G. Hewson, D. J. Longridge, A. G. Muddle, and D. F. Sarphie, "Transdermal and transmucosal powdered drug delivery." *Critical Reviews in Therapeutic Drug Carrier Systems*, vol. 16, no. 4, pp. 331–384, 1999. 1.2

[16] D. Chen, R. L. Endres, C. A. Erickson, K. F. Weis, M. W. McGregor, Y. Kawaoka, and L. G. Payne, "Epidermal immunization by a needle-free powder delivery technology: Immunogenicity of influenza vaccine and protection in mice," *Nature Medicine*, vol. 6, no. 10, pp. 1187–1190, 10 2000. [Online]. Available: http://dx.doi.org/10.1038/80538 (document), 1.2, 2-3

[17] A. Ziegler, "Needle-free delivery of powdered protein vaccines: A new and rapidly developing technique," *Journal of Pharmaceutical Innovation*, vol. 3, pp. 204–213, 2008, 10.1007/s12247-008-9039-x. [Online]. Available: http://dx.doi.org/10.1007/s12247-008-9039-x 1.2, 3.5

[18] O. A. Shergold, N. A. Fleck, and T. S. King, "The penetration of a soft solid by a liquid jet, with application to the administration of a needle-free injection." *Journal of Biomechanics*, vol. 39, no. 14, pp. 2593–2602, 2006. [Online]. Available: http://www.ncbi.nlm.nih.gov/pubmed/16277987 (document), 2.1, 2-1, 2.3.1

[19] R. H. Wildnauer, J. W. Bothwell, and A. B. Douglass, "Stratum corneum biomechanical properties i. influence of relative humidity on normal and extracted human stratum corneum," *Journal of Investigative Dermatology*, vol. 56, no. 1, pp. 72–78, 01 1971. [Online]. Available: http://dx.doi.org/10.1111/1523-1747.ep12292018 2.1

[20] J. Schramm-Baxter and S. Mitragotri, "Needle-free jet injections: dependence of jet penetration and dispersion in the skin on jet power," *Journal of Controlled Release*, vol. 97, no. 3, pp. 527 – 535, 2004. [Online]. Available: http://www.sciencedirect.com/science/article/pii/S0168365904001853 (document), 2.1, 2.1, 2-2

[21] M. Kendall, F. Carter, T. Mitchell, and B. Bellhouse, "Comparison of the transdermal ballistic delivery of micro-particles into human and porcine skin," in *Engineering in Medicine and Biology Society, 2001. Proceedings of the 23rd Annual International Conference of the IEEE*, vol. 3, 2001, pp. 2991 – 2994 vol.3. 2.2, 2.2

[22] J. A. Roberson and C. T. Crowe, *Engineering Fluid Mechanics*, 6th ed. John Wiley and Sons, 1997. 2.3.1

[23] R. H. Perry and D. W. Green, Eds., *Perry's Chemical Engineers' Handbook.* McGraw-Hill Co., 1984. 2.3.1

[24] J. E. Baumgardner, D. J. Graves, G. R. Neufeld, and J. A. Quinn, "Gas flux through human skin: effect of temperature, stripping, and inspired tension." *Journal of Applied Physiology*, vol. 58, no. 5, pp. 1536–1545, May 1985. 3.3

[25] A. Clausi, J. Cummiskey, S. Merkley, J. F. Carpenter, L. J. Braun, and T. W. Randolph, "Influence of particle size and antigen binding on effectiveness of aluminum salt adjuvants in a model lysozyme vaccine." *Journal of Pharmaceutical Sciences*, vol. 97, no. 12, pp. 5252–5262, Dec 2008. 3.5

[26] 3D. Systems. (2012) 3d systems website. [Online]. Available: www.3dsystems.com 3.6.1

[27] R. Bird, W. Stewart, and E. Lightfoot, *Transport Phenomena.* John Wiley and Sons, 1960. 4.1.2

[28] V. Research. (2012) Vision research website. [Online]. Available: www.visionresearch.com/ 4.2.1

[29] MATLAB. (2012) Matlab website. [Online]. Available: www.mathworks.com 5.5

[30] J. C. Stachowiak, T. H. Li, A. Arora, S. Mitragotri, and D. A. Fletcher, "Dynamic control of needle-free jet injection," *Journal of Controlled Release*, vol. 135, no. 2, pp. 104 – 112, 2009. [Online]. Available: http://www.sciencedirect.com/science/article/pii/S0168365909000297 5.7

[31] I. Analyst. (2012) Matlab script for simple color detection. [Online]. Available: http://www.mathworks.com/matlabcentral/fileexchange/26420-simplecolordetection A.1

Appendix A

MATLAB Script for Tissue 3D Reconstruction

Selected MATLAB (Release 2011a) code is shown in this appendix. The code that is displayed takes a series of tissue cross section photographs and performs image processing and computes an isosurface to reconstruct the 3D shape of the powder dispersion in the tissue.

A.1 hsvtest.m

This piece of code reads one photograph of a tissue section and finds the 2D border of the powder dispersion by thresholding hue (h), saturation (s), and luminance value (v). This piece was adapted from [31] to threshold based on hue, value, and luminance, instead of red, green, and blue values.

```
figure;
a = 2537;
fontSize=13;

for i = a
%Read image named 'IMG_i.jpg'
```

```
I0 = imread(strcat('IMG_',num2str(i),'.JPG'));
[rgbImage storedColorMap] = imresize(I0,.1);
hsvImage = rgb2hsv(rgbImage);

    % Read in image into an array.
    [rows columns numberOfColorBands] = size(rgbImage);
    % If it's monochrome (indexed), convert it to color.
    % Check to see if it's an 8-bit image needed later for scaling).
    if strcmpi(class(rgbImage), 'uint8')
        % Flag for 256 gray levels.
        eightBit = true;
    else
        eightBit = false;
    end

    % Display the original image.
    subplot(3, 4, 1);
    imshow(rgbImage);
    drawnow; % Make it display immediately.
    if numberOfColorBands > 1
        title('Original Color Image', 'FontSize', fontSize);
        title(strcat('Original IMG', num2str(i)), 'FontSize', ...
            fontSize);
    else
        caption = sprintf('Original Indexed Image\n(converted to ...
            true color with its stored colormap)');
        title(caption, 'FontSize', fontSize);
    end

    % Extract out the hue, saturation, and value from the ...
       original image
    % into 3 separate 2D arrays, one for each component.
    hue = hsvImage(:, :, 1);
    saturation = hsvImage(:, :, 2);
    value = hsvImage(:, :, 3);

```

```
40      % Display them.
41      subplot(3, 4, 2);
42      imshow(hue);
43      title('Hue', 'FontSize', fontSize);
44      subplot(3, 4, 3);
45      imshow(saturation);
46      title('Saturation', 'FontSize', fontSize);
47      subplot(3, 4, 4);
48      imshow(value);
49      title('Luminance Value', 'FontSize', fontSize);
50
51      % Compute and plot the hue histogram.
52      hR = subplot(3, 4, 6);
53      [countsR, grayLevelsR] = imhist(hue);
54      %countsR: number of count for a particular gray Level
55      %grayLevelsR: 0 to 1
56
57      maxGLValueR = find(countsR > 0, 1, 'last');
58      maxCountR = max(countsR); %max number of pixel counts for ...
            given level
59      bar(countsR, 'r');
60      grid on;
61      xlabel('Gray Levels');
62      ylabel('Pixel Count');
63      title('Histogram of Hue', 'FontSize', fontSize);
64
65      % Compute and plot the saturation histogram.
66      hG = subplot(3, 4, 7);
67      [countsG, grayLevelsG] = imhist(saturation);
68      maxGLValueG = find(countsG > 0, 1, 'last');
69      maxCountG = max(countsG);
70      bar(countsG, 'g', 'BarWidth', 0.95);
71      grid on;
72      xlabel('Gray Levels');
73      ylabel('Pixel Count');
74      title('Histogram of Saturation', 'FontSize', fontSize);
```

```
75
76      % Compute and plot the value histogram.
77      hB = subplot(3, 4, 8);
78      [countsB, grayLevelsB] = imhist(value);
79      maxGLValueB = find(countsB > 0, 1, 'last');
80      maxCountB = max(countsB);
81      bar(countsB, 'b');
82      grid on;
83      xlabel('Gray Levels');
84      ylabel('Pixel Count');
85      title('Histogram of Luminance Value', 'FontSize', fontSize);
86
87      % Set all axes to be the same width and height.
88      % This makes it easier to compare them.
89      maxGL = max([maxGLValueR,  maxGLValueG, maxGLValueB]);
90      if eightBit
91              maxGL = 255;
92      end
93      maxCount = max([maxCountR,  maxCountG, maxCountB]);
94      axis([hR hG hB], [0 maxGL 0 maxCount]);
95
96      % Plot all 3 histograms in one plot.
97      subplot(3, 4, 5);
98      plot(grayLevelsR, countsR, 'r', 'LineWidth', 2);
99      grid on;
100     xlabel('Gray Levels');
101     ylabel('Pixel Count');
102     hold on;
103     plot(grayLevelsG, countsG, 'g', 'LineWidth', 2);
104     plot(grayLevelsB, countsB, 'b', 'LineWidth', 2);
105     title('Histogram of All Bands', 'FontSize', fontSize);
106     maxGrayLevel = max([maxGLValueR, maxGLValueG, maxGLValueB]);
107     % Trim x-axis to just the max gray level on the bright end.
108     xlim([0 1])
109
110     % Now select thresholds for the 3 color bands.
```

```
111     % Assign the low and high thresholds for each color band.
112
113         % Take a guess at the values that might work for the ...
                user's image.
114         hueThresholdLow = graythresh(hue);
115         hueThresholdHigh = 1;
116         saturationThresholdLow = graythresh(hue);
117         saturationThresholdHigh = 1;
118         valueThresholdLow = .2;
119         valueThresholdHigh = graythresh(hue);
120
121     value1=im2bw(value,valueThresholdLow);
122     value2=im2bw(value,valueThresholdHigh);
123     value2=¬value2;
124     valueT=uint8(value1 & value2);
125
126     % Display them.
127     subplot(3, 4, 2);
128     imshow(im2bw(hue,hueThresholdLow));
129     title('Hue', 'FontSize', fontSize);
130     subplot(3, 4, 3);
131     imshow(im2bw(saturation,saturationThresholdLow));
132     title('Saturation', 'FontSize', fontSize);
133     subplot(3, 4, 4);
134     imshow(valueT,[]);
135     title('Luminance Value', 'FontSize', fontSize);
136
137     % Now apply each color band's particular thresholds to the ...
            color band
138     hueMask = (hue ≥ hueThresholdLow) & (hue ≤ hueThresholdHigh);
139     saturationMask = (saturation ≥ saturationThresholdLow) & ...
            (saturation ≤ saturationThresholdHigh);
140     valueMask = (value ≥ valueThresholdLow) & (value ≤ ...
            valueThresholdHigh);
141
142     %powderObjectsMask = uint8(hueMask);
```

```
143     powderObjectsMask = uint8(hueMask & saturationMask & valueMask);
144
145     % Tell user that we're going to filter out small objects.
146     smallestAcceptableArea = 1; % Keep areas only if bigger than ...
            this.
147
148     % Get rid of small objects.  Note: bwareaopen returns a logical.
149     powderObjectsMask = uint8(bwareaopen(powderObjectsMask, ...
            smallestAcceptableArea));
150
151     % Smooth the border using a morphological closing operation, ...
            imclose().
152     structuringElement = strel('disk', 4);
153     powderObjectsMask = imclose(powderObjectsMask, ...
            structuringElement);
154
155 [B,L] = bwboundaries(powderObjectsMask,'holes');
156
157 rgbImage1 = rgbImage;
158 for k = 1:length(B)
159     boundary = B{k};
160          x=boundary(:,1);
161          y=boundary(:,2);
162          for k1=1:length(B{k});
163              rgbImage1(x(k1),y(k1),:) = 0;
164          end
165 end
166 subplot(3, 4, 9);
167 imshow(rgbImage1);
168 title(strcat('Image + Border: thresh = ...
        ',num2str(saturationThresholdLow)),'FontSize', fontSize);
169
170
171 subplot(3, 4, 10);
172   for k=1:length(B)
173       boundary = B{k};
```

```
174         z=15*(a(length(a))+1-i)+boundary(:,2)-boundary(:,2);
175         y=9.4*(rows-boundary(:,1));
176         plot3(9.4*boundary(:,2), y(:), z(:));
177         hold on
178       end
179     end
180
181     xlabel('\mum');
182      ylabel('\mum');
183      zlabel('\mum');
184      title('Title','FontSize', fontSize);
```

A.2 injectionshape.m

This piece of code thresholds a series of tissue section photographs based on an hsv threshold and computes and plots an 3D isosurface to yield the 3D shape of the powder dispersion in the tissue.

```
1  % This version tries out isosurface, smooth3, to obtain a smooth ...
       3D surface
2  % I also store thresholded points representing powder as a 3D array
3  % instead of directly plotting or calculating its volume.
4
5  clear;
6  a = [2507:2537];
7  fontSize=13;
8  um_pixel = 18.18; %conversion from pixel to um
9  z_index=length(a);
10
11 for i = a
12 %will read an series of photos, in this case: IMG_2507.jpg to ...
       IMG_2537.jpg
13      I0 = imread(strcat('IMG_',num2str(i),'.JPG'));
14 [rgbImage storedColorMap] = imresize(I0,.1);
```

```
15 hsvImage = rgb2hsv(rgbImage);
16
17     % Read in image into an array.
18     [rows columns numberOfColorBands] = size(rgbImage);
19     % If it's monochrome (indexed), convert it to color.
20     % Check to see if it's an 8-bit image needed later for scaling).
21     if strcmpi(class(rgbImage), 'uint8')
22         % Flag for 256 gray levels.
23         eightBit = true;
24     else
25         eightBit = false;
26     end
27
28     hsvImage = ...
           hsvImage((rows-round(4200/um_pixel)):(rows-round(2800/um_pixel)),(round(45
29     axis([4500 6200 2800 4200 0 500]);
30
31     % Extract out the hue, saturation, and value from the ...
           original image
32     % into 3 separate 2D arrays, one for each component.
33     hue = hsvImage(:, :, 1);
34     saturation = hsvImage(:, :, 2);
35     value = hsvImage(:, :, 3);
36
37     % Now select thresholds for the 3.
38     % Assign the low and high thresholds for each.
39
40         % Use threshold values from graythresh of IMG_9901.
41         hueThresholdLow = .2; %.3804;
42         hueThresholdHigh = 1;
43         saturationThresholdLow = 0.01; %.3412;
44         saturationThresholdHigh = 1;
45         valueThresholdLow = .2;
46         valueThresholdHigh = .65;
47
48     % Now apply each band's particular thresholds to the band
```

```
49      hueMask = (hue ≥ hueThresholdLow) & (hue ≤ hueThresholdHigh);
50      saturationMask = (saturation ≥ saturationThresholdLow) & ...
            (saturation ≤ saturationThresholdHigh);
51      valueMask = (value ≥ valueThresholdLow) & (value ≤ ...
            valueThresholdHigh);
52
53      powderObjectsMask = uint8(hueMask & saturationMask & valueMask);
54
55      % Tell user that we're going to filter out small objects.
56      smallestAcceptableArea = 1; % Keep areas only if they're ...
            bigger than this.
57
58      % Get rid of small objects.  Note: bwareaopen returns a logical.
59      powderObjectsMask = uint8(bwareaopen(powderObjectsMask, ...
            smallestAcceptableArea));
60
61      % Smooth the border using a morphological closing operation, ...
            imclose().
62      structuringElement = strel('disk', 4);
63      powderObjectsMask = imclose(powderObjectsMask, ...
            structuringElement);
64
65      store(:, :, z_index) = powderObjectsMask(:,:);
66      z_index = z_index-1;
67  end
68
69      dimensions=size(powderObjectsMask);
70      x_length=dimensions(2);
71      y_length=dimensions(1);
72
73      smstore = smooth3(store, 'box', 3);
74
75      x=[0:um_pixel:um_pixel*(x_length-1)];
76      y=[0:um_pixel:um_pixel*(y_length-1)];
77      z=[-15*(length(a)-1):15:0];
78
```

```
79      figure;
80      p = patch(isosurface(x,y,z,smstore));
81      isonormals(x,y,z,smstore,p);
82      set(p,'FaceColor',[.161 .249 .886],'EdgeColor','none');
83      camlight;
84      axis vis3d
85      lighting phong
86      daspect([1 1 1]);
87
88      xlabel('\mum');
89      ylabel('\mum');
90      zlabel('\mum');
91      view(0,20);
```

Appendix B

CAD of the Aluminum Alloy Nozzle

All dimensions in mm.

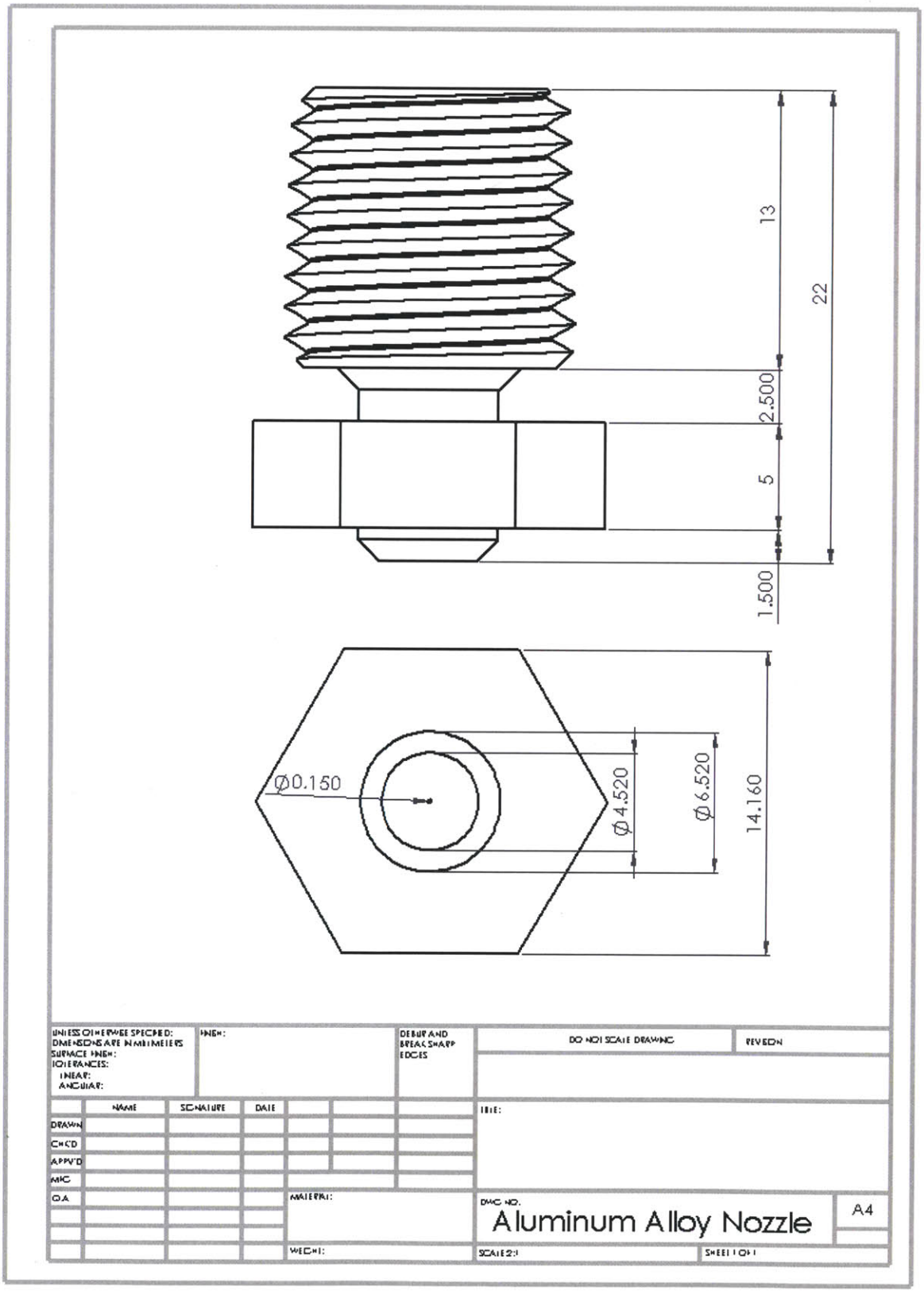
13
22
2.500
5
1.500
Ø0.150
Ø4.520
Ø6.520
14.160
UNLESS OTHERWISE SPECIFIED:
DIMENSIONS ARE IN MILLIMETERS
SURFACE FINISH:
TOLERANCES:
LINEAR:
ANGULAR:
FINISH:
DEBURR AND BREAK SHARP EDGES
DO NOT SCALE DRAWING
REVISION
NAME
SIGNATURE
DATE
DRAWN
CHK'D
APPV'D
MFG
Q.A
MATERIAL:
WEIGHT:
TITLE:
DWG NO.
Aluminum Alloy Nozzle
A4
SCALE:1
SHEET 1 OF 1